

EPR OF Mn^{2+} IMPURITIES IN BLODITE
AND NEWBERYITE NATURAL MINERALS

by

Barry R. Kiggins

Submitted in partial fulfillment
of the requirements for the degree of
Master of Science

Department of Physics
Faculty of Science and Engineering
University of Ottawa
OTTAWA, Canada.

Abstract

The electron paramagnetic resonance of Mn^{2+} impurities in natural crystals of blodite, $2(Na_2Mg(SO_4)_2 \cdot 4H_2O)$, and newberyite, $8(MgHPO_4 \cdot 3H_2O)$, was studied in the 9.2 GHz microwave frequency range and at room temperature. In each mineral, two differently oriented, but otherwise equivalent, magnetic complexes of Mn^{2+} were found. The complexes were related to each other by two-fold symmetry about the crystallographic b axis. The resonance line positions were fitted to a spin Hamiltonian of rhombic symmetry. For blodite, the following parameters were determined: $g = 1.9993$ (5), $b_2^0 = 334.0$ (1.5), $b_2^2 = 260.0$ (1.5), $b_4^0 = 1.2$ (.2), $A = 89.0$ (1.0) and $B = 86.4$ (.5). For newberyite, the parameters were: $g = 1.9995$ (5), $b_2^0 = 253.5$ (1.5), $b_2^2 = 252.0$ (1.5), $b_4^0 = -0.79$ (.10), $A = 89.7$ (1.5) and $B = 88.2$ (1.5). The values of b_m^n , A and B are in units of 10^4 cm^{-1} . The possible significance of the size of the A and B hyperfine parameters is discussed. The EPR results for newberyite are compared to those obtained for struvite, which is a mineral that can decompose into newberyite. In addition, the optical absorption of Mn^{2+} in blodite was studied at room temperature. The line positions were fitted to crystal field matrices of interaction and the crystal field parameters determined.

Table of Contents

| | | |
|-------------------|--|------|
| ABSTRACT | | i |
| TABLE OF CONTENTS | | ii |
| ACKNOWLEDGEMENTS | | iv |
| LIST OF FIGURES | | v |
| LIST OF TABLES | | viii |
| CHAPTER I | INTRODUCTION | 1 |
| CHAPTER II | CRYSTALLOGRAPHY | 6 |
| | A. BLODITE | 6 |
| | B. NEWBERYITE | 8 |
| | C. QUALITY OF THE CRYSTALS. | 11 |
| CHAPTER III | THEORY | 12 |
| | A. CRYSTAL FIELD THEORY | 12 |
| | B. EPR THEORY | 23 |
| | a) Zeeman Interaction | 23 |
| | b) Hyperfine Interaction | 25 |
| | c) The Spin Hamiltonian | 28 |
| | d) EPR Transitions for Mn^{2+} in Blodite and Newberyite | 32 |
| | e) S-state Zero-Field Splitting | 36 |

| | | |
|--------------------|--|-----|
| CHAPTER IV | EQUIPMENT | 50 |
| | A. OPERATING PRINCIPLES OF X-BAND SPECTROMETER | 50 |
| | B. X-BAND CAVITY | 55 |
| | C. MAGNETIC FIELD MEASUREMENTS | 58 |
| | D. OPTICAL SPECTROMETER | 59 |
| | E. OPTICAL MEASUREMENTS | 59 |
| CHAPTER V | EXPERIMENTAL PROCEDURE AND RESULTS | 62 |
| | A. EPR OF BLODITE | 62 |
| | B. EPR OF NEWBERYITE | 75 |
| | C. OPTICAL ABSORPTION OF BLODITE | 84 |
| CHAPTER VI | CONCLUSIONS | 95 |
| | A. EPR OF BLODITE AND NEWBERYITE | 95 |
| | B. OPTICAL ABSORPTION OF BLODITE | 102 |
| APPENDIX | | 107 |
| LIST OF REFERENCES | | 124 |
| CURRICULUM VITAE | | 129 |

Acknowledgments

The author wishes to thank Dr. Armen Manoogian for suggestion of the topic and for very encouraging and meaningful guidance during the course of the research. Special thanks are also due Mr. B. W. Chan for his very able technical assistance in the operation of the EPR equipment. Mr. O. Berolo for his technical assistance on the optical spectrometer and Mr. J. F. Rowland of the Department of Energy, Mines and Resources, Ottawa, for precision camera X-ray measurements. Financial assistance from Dr. A. Manoogian's National Research Council grant is gratefully acknowledged. I wish to thank Miss L. Sawyer for the typing of this thesis.

List of Figures

1. Unit cell of blodite showing a) projection on the (010) plane, and b) projection on the (100) plane, with the projection parallel to c. Z_a and Z_b represent the two choices for the orientation of a Z magnetic axis of Mn^{2+} . 7
2. Unit cell of newberyite projected on the (010) plane. 10
3. Splitting of the d-orbitals by a cubic crystal field (taken from Pratt and Coelho¹⁷). 14
4. Block diagram of the klystron power supply 52
5. Block diagram of the X-band spectrometer. 54
6. X-band cavity a) iris, b) modulation coil, c) sample, d) perspex pin e) lower pulley, f) string. 56
7. Block diagram of the optical absorption apparatus. 60
8. Stereogram showing the relationship between the Mn^{2+} magnetic axis and the crystalline axes for blodite 63

9. The spectrum of Mn^{2+} in blodite along a magnetic z axis. 66
10. Angular variation in position of Mn^{2+} hyperfine lines in blodite as magnet is rotated from a z to a y magnetic axis. 67
11. Energy level diagram of Mn^{2+} in blodite along a magnetic z axis 71
12. Energy level diagram of Mn^{2+} in blodite along a magnetic y axis. 72
13. Energy level diagram of Mn^{2+} in blodite along a magnetic x axis. 73
14. Hyperfine energy level diagram of Mn^{2+} in blodite along a magnetic z direction. 74
15. Spectrum of Mn^{2+} in newberyite along a magnetic z direction. 76
16. Spectrum of Mn^{2+} in struvite along a magnetic z direction. 77
17. Stereogram showing relationship between the Mn^{2+} magnetic axis and the crystallographic axes for newberyite. 78
18. Energy level diagram of Mn^{2+} in newberyite along a magnetic z axis. 82
19. Energy level diagram of Mn^{2+} in newberyite along a magnetic y axis. 83

20. Optical absorption spectrum of Mn^{2+} in blodite. 85
21. Crystal field diagram of Mn^{2+} in blodite 89
22. Splitting of ${}^4A_{1g}$ 4E_g (4G) level as a function of ϵ . 91
23. Crystal field diagram of Mn^{2+} in blodite including covalency. 93
24. Monotomic plot of the hyperfine interaction constant A of Mn^{2+} versus the covalency parameter c divided into the number of ligand n (taken from Simanek and Muller⁷). 99
- a - coordination of $6O^{2-}$
 - b - coordination of $6H_2O$
 - c - coordination of $4H_2O.2O^{2-}$
 - d - coordination of $6F^-$
 - e - coordination of $3H_2O.3O^{2-}$

List of Tables

| | | |
|-------|--|-------|
| I. | Electronic Energies of Some States of the Mn^{2+} Free Ion | 16 |
| II. | Electronic Energy Levels of Mn^{2+} in a crystalline Field of Cubic Symmetry. | 17 |
| III. | Energy Matrices in the Strong Field Representation including the Effects of Covalency | 21,22 |
| IV. | Relationship between the parameters of the spin Hamiltonian for different orientations of the Magnetic Field H. | 35 |
| V. | Values of α_i , β_i , γ_i and Δ_i for the Mn^{2+} ion at $10Dq = 10000 \text{ cm}^{-1}$. | 43 |
| VI. | Crystal Field Parameters of B_m^n . | 48 |
| VII. | Contribution to D and E from various mechanisms. | 49 |
| VIII. | Angular Relationships between the Magnetic and Crystallographic Axes of Mn^{2+} in Blodite. | 64 |

| | | |
|-------|---|----|
| IX. | Magnetic Field positions of the lowest EPR lines for each of the hyperfine groups of Mn^{2+} in blodite. | 69 |
| X. | Spin Hamiltonian parameters of Mn^{2+} in blodite. | 70 |
| XI. | Angular Relationships between the Magnetic and Crystallographic Axes of Mn^{2+} in Newberyite. | 79 |
| XII. | Magnetic Field positions of the lowest EPR lines for each of the hyperfine groups of Mn^{2+} in newberyite. | 80 |
| XIII. | Spin Hamiltonian parameters of Mn^{2+} in newberyite and struvite | 81 |
| XIV. | Optical Absorption Peaks of Mn^{2+} in blodite. | 87 |
| XV. | Predicted and observed energy level values of Mn^{2+} in blodite. | 90 |
| XVI. | Comparison of calculated and observed line positions in the optical spectrum of Mn^{2+} in blodite at $10Dq' = 11000 \text{ cm}^{-1}$ and $\epsilon = 0.04$. | 94 |

| | | |
|--------|---|-------|
| XVII. | Some g-values for Mn^{2+} in various compounds | 96,97 |
| XVIII. | Comparison of hyperfine parameters for Mn^{2+} in some crystals. | 100 |
| XIX. | Comparison of Optical Absorption Line Positions of Mn^{2+} in various Compounds. | 103 |
| XX. | Comparison of Crystal Field Parameters in various Crystals. | 105 |

Chapter I

Introduction

The effect of a crystalline environment on the energy levels of a paramagnetic ion can be studied by employing the techniques of electron paramagnetic resonance (EPR) and optical absorption. EPR gives an accurate description of the ground state of the ion while optical absorption gives information about the higher energy levels. The study is of particular interest for the case of Mn^{2+} impurities since the divalent manganese ion is found quite frequently in many natural minerals. Hence, by obtaining data for Mn^{2+} impurities in different crystals, one is able to correlate the results and to ascertain some aspects of the behaviour of the minerals. The manganese impurities often exist in crystal sites which are coordinated by distorted octahedrons of negatively charged ions. These ions interact with the paramagnetic impurity and cause the energy levels of the impurity to split.

While many EPR and optical absorption studies have been reported for Mn^{2+} ions coordinated by ligands of $6.O^{2-}$ or by $6.H_2O$, we have studied the manganese ions coordinated by mixed ligands of

oxygens and waters. The natural minerals studied are blodite, $2(\text{Na}_2\text{Mg}(\text{SO}_4)_2 \cdot 4\text{H}_2\text{O})$ and newberyite, $8(\text{MgHPO}_4 \cdot 3\text{H}_2\text{O})$. These crystals have Mn^{2+} impurities on sites with coordinated ligands of $(2\text{O}^{2-} + 4\text{H}_2\text{O})$ and $(3\text{O}^{2-} + 3\text{H}_2\text{O})$, respectively. EPR studies were performed on both of the crystals, but only blodite was of sufficient quality to permit optical absorption studies.

The Mn^{2+} free ion has a ground state described by $3d^5$, ${}^6\text{S}_{5/2}$, and so this state is six-fold degenerate with respect to the magnetic quantum number M_S , with values of $M_S = \pm 5/2, \pm 3/2, \pm 1/2$. In an octahedral crystalline electric field the ground state is described by the term $(t_{2g})^3(e_g)^2$, ${}^6\text{A}_{1g}$. The upper levels are either quartets or doublets. The effect of the crystalline electric field is to remove the degeneracy either wholly or in part. This effect, commonly known as zero field splitting, is present in all experiments published to date.

To theoretically calculate the zero field splitting the energies of the higher quartets must be found by optical methods. However, optical absorption signals due to a $3d^5$ electron configuration are weak since they are both spin forbidden and direct electric dipole forbidden (Burns¹). They are spin forbidden because the ground state

is a sextet and the higher energy levels are either quartets or doublets. But, by various small interactions, such as spin-orbit coupling, the states become mixed and the spin forbidden condition is relaxed. They are direct electric dipole forbidden because all the energy levels are of even parity, and an electric dipole transition requires a change of parity. But through vibronic effects, Koide and Pryce² have shown that electric dipole transitions can occur with the excitation of one quantum (or an odd number) of an odd vibration. Other possible mechanisms for transitions are magnetic dipole, electric quadrupole and ion-phonon interactions. Koide and Pryce² also point out the effects of covalency on the optical spectra by considering the overlap of the e_g orbitals of the paramagnetic ion with the ligand σ orbitals.

Several studies have been reported which attempt to correlate bonding in the coordinated manganese complexes using the parameters derived from EPR measurements. Owen³ considered the influence of covalent bonding on the paramagnetic resonance of the hydrated ion group. Manganese has a $(t_{2g})^3(e_g)^2$ configuration and, according to Owen, the t_{2g} electrons form molecular π -bonds with the $2P\pi$ electrons of adjacent oxygen ions while the $(e_g)^2$ electrons form σ -bonds with the $2P\sigma$ and $2s$ electrons of the oxygen ions. The effect of such

bonding is similar to the effect produced by increasing the crystal field strength (and hence the cubic field splitting).

An empirical relation exists (Van Wieringen⁴) between the amount of covalent bonding and the magnitude of the hyperfine splitting. The dependence is such that an increase in covalent bonding corresponds to a decrease in the hyperfine splitting. Matumura⁵ plotted percent ionicity against the hyperfine splitting parameter, A, for various host lattices. It is possible to use his curve to obtain an estimate of the amount of covalency of Mn^{2+} in a particular crystal. Further reports by Henning⁶ and Simanek and Muller⁷ have been published relating the covalency, according to Pauling's⁸ definition, to the hyperfine splitting. Pauling's parameter is based on the electronegativity property, which is the power of an atom in a molecule to attract electrons to itself. Phillips⁹ pointed out that there is no exact theory for bonding, and so Pauling's definitions rest on some assumptions which make the results only approximate. Nevertheless they do provide a useful method for correlating the parameter A to the bonding at the paramagnetic site. Phillips also showed that spin-orbit splittings may serve as a measure of ionicity but the accuracy of such an approach is in doubt.

EPR measurements were obtained for blodite and newberyite using a commercial X-band spectrometer operating at the 9.2 GHz microwave frequency range. All measurements were done at room temperature. The resonance line positions in both crystals were fitted to a spin Hamiltonian with rhombic symmetry. Using the values of the constants found for the Hamiltonians, and with the aid of a computer, it was possible to plot the energy levels as a function of the externally applied magnetic field. The magnitudes of the hyperfine parameters obtained were used to correlate the covalencies of the occupied sites in the two crystals with the types of ligands surrounding the paramagnetic ion. The crystal field parameters were calculated using the optical data and an estimate of the covalency was again determined and discussed. The lack of precision in the published theoretical predictions of S-state splitting did not allow use of the optical data obtained to calculate the ground state splitting. However, it was possible to do a point charge calculation of the potential at the Mn^{2+} site in blodite since the positions of the atoms in the unit cell of blodite are accurately known. From such potential information, one can calculate an estimate of the zero field splitting parameters D and E using an appropriate theoretical model and then compare these parameters to the values obtained from the EPR calculations.

Chapter II

Crystallography

A. Blodite

Blodite (also called astrakhanite) has the formula $2(\text{Na}_2\text{Mg}(\text{SO}_4)_2 \cdot 4\text{H}_2\text{O})$. It is monoclinic with space group $P2_1/a \cong C_{2h}^5$. The first notation indicates a primitive lattice with glide planes parallel to (010) combined with screw diad axes parallel to the crystallographic y axis.

Schoenflies' notation yields similar information, the 2 referring to the two-fold rotation axis and the h to a horizontal plane of symmetry perpendicular to this axis; the superscript 5 means it is the fifth available monoclinic space group.

The crystallography of Zn-blodite, where Zn has replaced Mg, has been done by Giglio¹⁰. A refined X-ray study of blodite was done by Rumanova and Malitskaya¹¹; these authors called the mineral astrakhanite. The unit cell dimensions are given as $a = 11.03$,

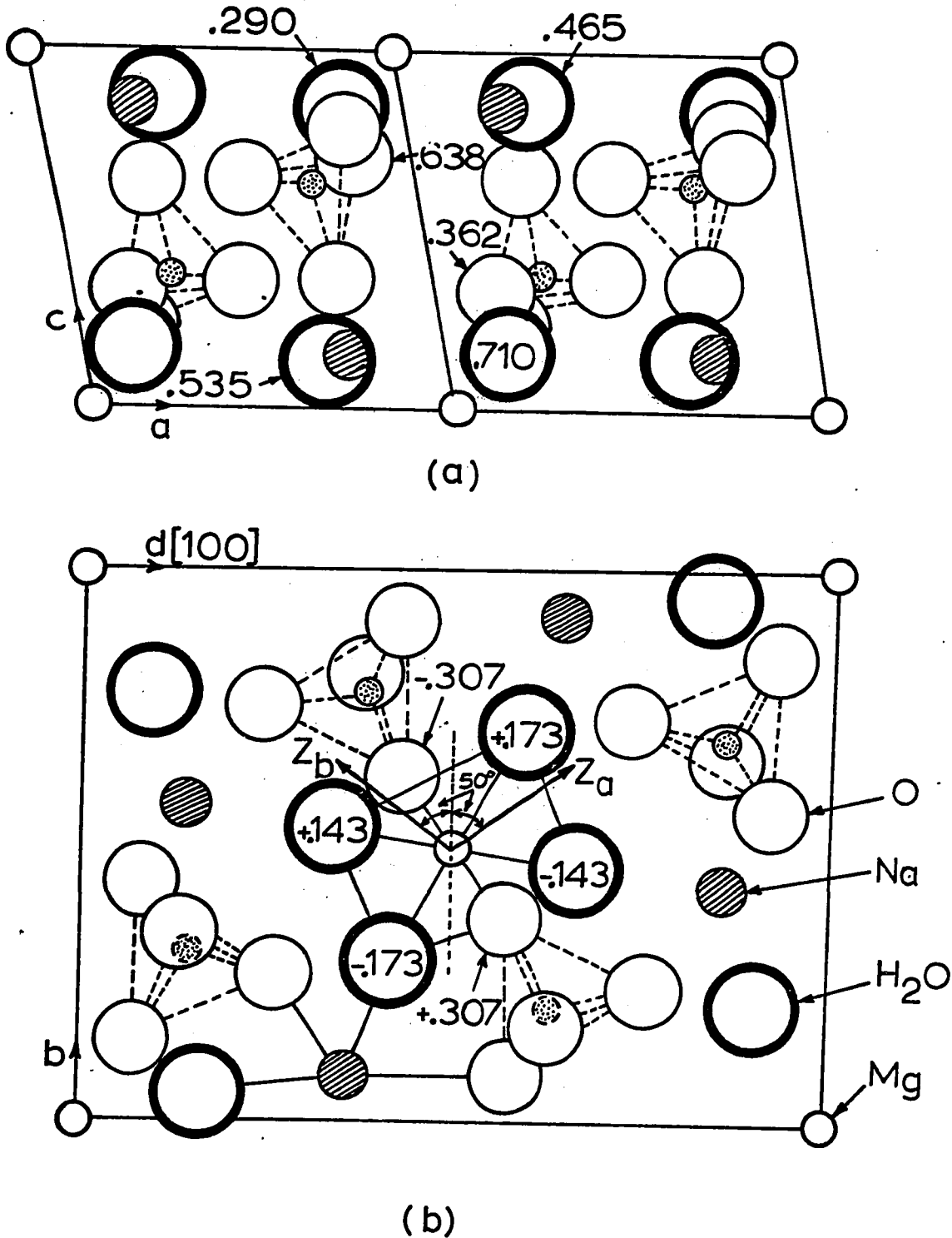


Figure 1. Unit cell of blodite showing a) projection on the (010) plane, and b) projection on the (100) plane, with the projection parallel to c. Z_a and Z_b represent the two choices for the orientation of a Z magnetic axis of Mn²⁺.

$b = 8.14$, $c = 5.49 \text{ \AA}$ and $\beta = 100^\circ 40'$. The unit cell is shown in Figure 1, based on the data given by Rumanova and Malitskaya.

Figure 1 is similar to the one produced by Giglio but the atom positions differ somewhat for astrakhanite. The Mn^{2+} ion substitutes for Mg^{2+} in an octahedral environment of four water molecules and two oxygen. There are two magnesium sites per unit cell related by two-fold symmetry about the b-axis.

B. Newberyite

Newberyite is an interesting mineral in that it is found in both geological and biological deposits. In the first case, it is found as a constituent of bat guano; and in the second case as a constituent of urinary and bladder calculi. In all instances, newberyite has been found as a product of the decomposition of struvite (also called guanite). There is a possibility that newberyite can form independently from struvite, but no evidence to this effect has yet been found. It is informative in this work to discuss struvite whenever newberyite is discussed since EPR data is available for struvite.

Newberyite has the formula $\text{MgHPO}_4 \cdot 3\text{H}_2\text{O}$ and has eight molecules per unit cell. It belongs to the orthorhombic space group Pbcu.

The symbols a, b and c refer to glide planes and denote the direction of the glide component. The crystal structure of newberyite has been analyzed by Sutor¹² and the cell dimensions are given as a = 10.215, b = 10.681 and c = 10.014 Å.

Struvite has the formula $\text{MgNH}_4\text{PO}_4 \cdot 6\text{H}_2\text{O}$ with two molecules per unit cell, and it may be related to newberyite by the following chemical formula¹³:



Struvite is also orthorhombic belonging to the space group $\text{Pmn}2_1$. The two m's in this notation indicate mirror planes perpendicular to the a and b crystallographic directions and 2_1 indicates a screw diad perpendicular to the c direction. The crystal structure of struvite was determined by Whitaker and Jeffrey^{14,15}, and the cell dimensions are given as a = 6.941, b = 6.137 and c = 11.199 Å.

In both newberyite and struvite the paramagnetic ion Mn^{2+} substitutes as an impurity in the magnesium sites. Both sites are coordinated with atoms or molecules forming a distorted octahedron. The Mn^{2+} ions in newberyite are surrounded by three oxygens and three water molecules while in struvite by six water molecules. The crystal structure of newberyite projected on the (010) plane is

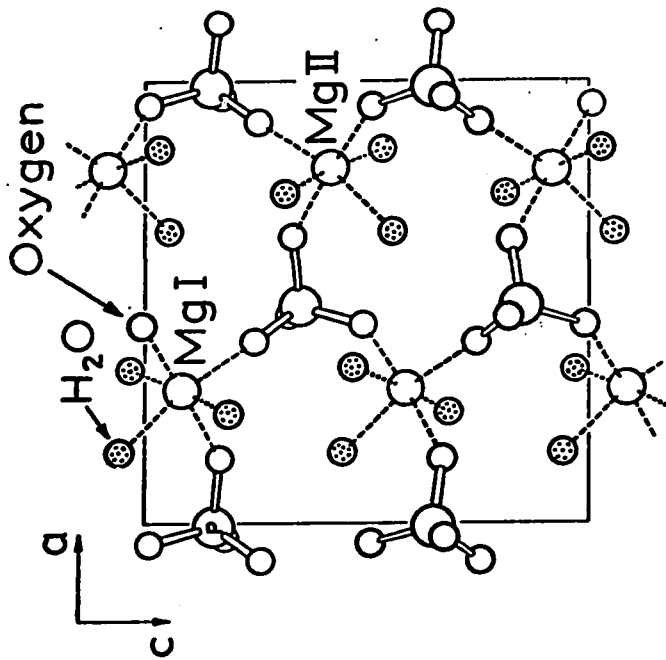


Figure 2. Unit cell of newberyite projected on the (010) plane.

shown in Figure 2. The bonding picture of struvite is complicated by the strong bonding of some of the manganese coordinated waters to other atoms in the unit cell. In both newberyite and struvite there are two inequivalent magnesium sites in the unit cell. In Figure 2, for newberyite, the sites are marked Mg_I and Mg_{II} . The magnesium sites in newberyite are related by two-fold symmetry about the crystallographic b direction.

C. Quality of the Crystals

The blodite crystals originated from the Soda Lake region of California. They were of good quality and had dimensions of about $1'' \times 1'' \times 3/8''$. A chip with dimensions of about $(1/8'')^3$ was used for the EPR studies. Slices of approximately $1/16''$ thick were used for optical absorption studies. The newberyite crystals originated from the Skipton caves, Victoria, Australia. They were of fair quality and had well-defined faces. A typical crystal had dimensions of $5/16'' \times 1/4'' \times 3/16''$. While no EPR measurements were done on struvite, Mn^{2+} resonance lines were observed in this crystal. This crystal also originated from the Skipton caves. It was white and had well-defined faces. The dimensions were approximately $(1/4'')^3$.

Chapter III

Theory

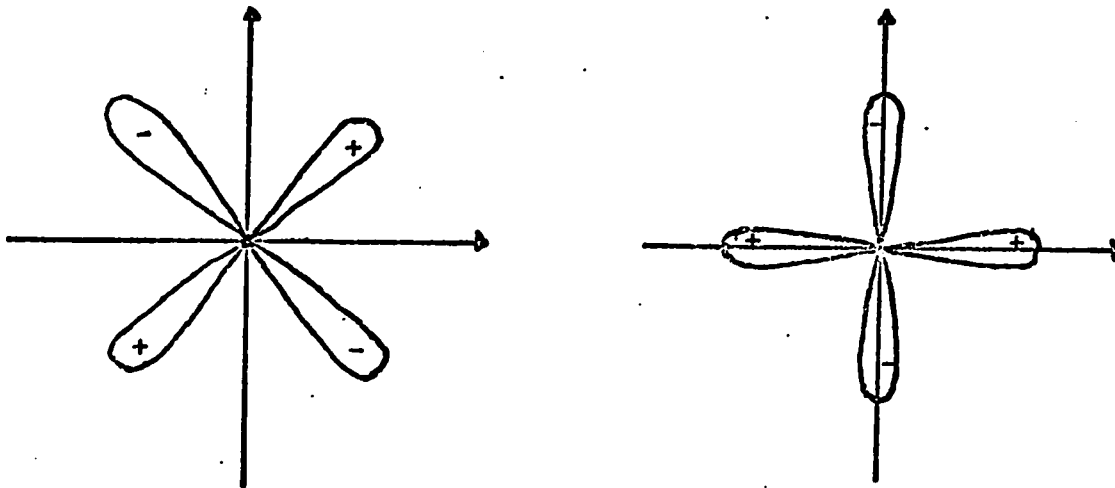
A. Crystal Field Theory

Crystal field theory rests on the assumption that the paramagnetic ion resides in an electric field due to point charges or point dipoles lying wholly outside the paramagnetic ion. The interaction energy between the neighbouring charges and the paramagnetic ion is added to the Hamiltonian of the free ion in order to calculate the new energy levels. The crystalline potential, or field, has the symmetry of the neighbouring charges, and this symmetry fixes the properties of the ionic energy states.

Mn^{2+} has a $3d^5$ electron configuration. The d orbitals are designated by d_{xy} , d_{yz} , d_{xz} , $d_{x^2 - y^2}$, and d_{z^2} , and each orbital has four lobes at right angles. The d_{z^2} orbital is a combination of two other orbitals $d_{z^2 - y^2}$ and $d_{z^2 - x^2}$ ¹⁶. The sign of the wave function for lobes in opposite quadrants is identical but opposite to that of lobes in adjacent quadrants. The five d orbitals

are divided into two groups on the basis of their angular distributions. Three of the orbitals, d_{xy} , d_{yz} and d_{xz} , have lobes projecting between the cartesian axes, and they are denoted by group theory as t_{2g} . In this notation t refers to the three-fold degeneracy, the subscript 2 indicates that the wave function does not change sign on rotation about the axes diagonal to the cartesian axes, and the subscript g refers to the fact that the wave function does not change sign upon inversion (even parity, symmetric wave functions). The two other orbitals, $d_{x^2 - y^2}$ and d_{z^2} , have lobes directed along the cartesian axes. They are designated e_g , where e stands for two-fold degeneracy. In an octahedral crystal field, the two groups are split by an amount $10 Dq$, where Dq is defined as the constant in the cubic field potential. This information is summarized in Figure 3 (Pratt and Coelho¹⁷).

The free ion states of Mn^{2+} include a ground state sextet, 6S , and nearest to it are several upper quartet levels, 4G , 4P , 4D and 4F . The energy values for the quartets are usually given in terms of Racah parameters B and C ¹⁸. The parameters B and C represent the electrostatic interactions between the d -electrons. They are defined by Racah as $B = F_2 - 5F_4$ and $C = 35F_4$, where the F 's are the Slater integrals¹⁹. The definitions for B and C are more convenient



$$t_{2g} \begin{cases} xy/r^2 \\ yz/r^2 \\ zx/r^2 \end{cases}$$

$$e_g \begin{cases} (x^2 - y^2)/r^2 \\ (2z^2 - x^2 - y^2)/r^2 \end{cases}$$

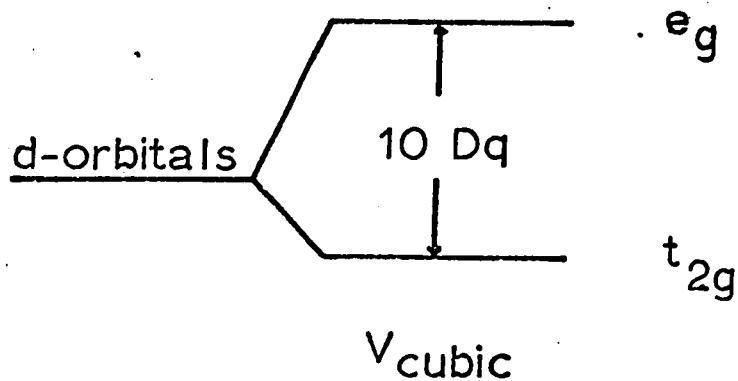


Figure 3. Splitting of the d-orbitals by a cubic crystals field (taken from Pratt and Coelho¹⁷).

to use than are the Slater integrals because the coefficients of these parameters are integers in the expressions for the energy levels arising from the d^n configuration. Table I gives the energy of the quartets based on a value of zero for the ground state (Heidt, Koster and Johnson²⁰).

When the Mn^{2+} ion is placed in a crystal field, the potential of this field splits the free ion states to produce various crystal field states. In a pure octahedral environment, the ground state is split into a four-fold level and a two-fold level. A reduction of the field symmetry to orthorhombic splits the ground state into three doublets known as Kramer's doublets. Kramer's theorem states that a purely electrostatic field acting on a system of an odd number of electrons can never reduce the degeneracy below two. Low²¹ described how this degeneracy is related to the invariance of the system under time reversal.

The upper quartet states are split by the crystal field to a very much greater extent than is the ground state. Table II gives the energy states of the ion which are derived from the free ion states and their relative energies in a cubic crystal field.

Table I: Electron Energies of Some States of the Mn^{2+} Free Ion

| State | Energy in terms of Racah parameters |
|----------------|--|
| ${}^6\text{S}$ | 0 |
| ${}^4\text{G}$ | $10\text{B} + 5\text{C}$ |
| ${}^4\text{P}$ | $7\text{B} + 7\text{C}$ |
| ${}^4\text{D}$ | $17\text{B} + 5\text{C}$ |
| ${}^4\text{F}$ | $22\text{B} + 7\text{C}$ |

Table II: Electronic Energy Levels of Mn^{2+} in a Crystalline Field of Cubic Symmetry

| Level of free ion | Level of ion in field | Energy |
|-------------------|-----------------------|-----------------|
| 6S | ${}^6A_{1g}$ | |
| 4G | ${}^4T_{1g}$ | $< {}^4T_{2g}$ |
| | ${}^4T_{2g}$ | $< {}^4G$ |
| | 4E_g | $\approx {}^4G$ |
| | ${}^4A_{1g}$ | $\approx {}^4G$ |
| 4P | ${}^4T_{1g}$ | $> {}^4P$ |
| 4D | ${}^4T_{2g}$ | $< {}^4D$ |
| | 4E_g | $\approx {}^4D$ |
| 4F | ${}^4A_{2g}$ | $\approx {}^4F$ |
| | ${}^4T_{1g}$ | $> {}^4F$ |
| | ${}^4T_{2g}$ | $> {}^4T_{1g}$ |

The symbols used to describe the energy levels of the ion produced in the crystal field are analogous to those used to describe the d-orbitals: the superscript refers to the spin multiplicity, T indicates three-fold spacial degeneracy, E indicates two-fold degeneracy, and A indicates non-degeneracy. The subscripts 2 and g have the same meaning as in the d-orbital group theory notation and the subscript 1 refers to mirror planes parallel to a symmetry axis. The three levels marked T_{1g} interact with each other as do the three levels marked T_{2g} and the two marked E_g . The levels ${}^4A_{1g}$ and ${}^4A_{2g}$ do not interact with any of the other levels or each other. The values of the new energy levels, E, are obtained by calculating the interaction between levels of the same symmetry in the presence of the octahedral field. Interaction matrices can be constructed and the energies E found from the roots of the secular determinant. These matrices have been given by Tanabe and Sugano²² and are given here for the levels with T_{1g} , T_{2g} , and E_g symmetries:

$$\begin{array}{c}
 {}^4T_{1g} ({}^4P, {}^4F, {}^4G) \\
 \left| \begin{array}{ccc}
 -10Dq + 10B + 6C - E & -3\sqrt{2} B & C \\
 -3\sqrt{2} B & 19B + 7C - E & -3\sqrt{2} B \\
 C & -3\sqrt{2} B & 10Dq + 10B + 6C - E
 \end{array} \right| = 0
 \end{array}$$

.....(1)

$${}^4T_{2g}({}^4F, {}^4G, {}^4D) \begin{vmatrix} -10Dq + 18B + 6C - E & \sqrt{6} B & 4B + C \\ \sqrt{6} B & 13B + 5C - E & -\sqrt{6} B \\ 4B + C & -\sqrt{6} B & 10Dq + 18B + 6C - E \end{vmatrix} = 0$$

.....(2)

$${}^4E_g({}^4D, {}^4G) \begin{vmatrix} 13B + 5C - E & -2\sqrt{3} B \\ -2\sqrt{3} B & 14B + 5C - E \end{vmatrix} = 0$$

.....(3)

The levels ${}^6A_{1g}$, ${}^4A_{1g}$, ${}^4A_{2g}$ and 4E_g do not depend on the strength of the crystal field, Dq ; mathematically, they have no matrix elements within themselves nor between other multiplets and themselves. The Racah parameters B and C can be found from the roots of equation (3), which are $10B + 5C$ and $17B + 5C$. It can be noted that the lowest 4E_g level is accidentally degenerate with the ${}^4A_{1g}$ level.

Equations (1), (2) and (3) represent the so-called strong field scheme in that the crystal field acting on each electron is considered

to be of cubic symmetry. This neglects non-cubic components of the field and also the spin-dependent forces which tend to further lift the degeneracy of the levels. The effect of spin-orbit and spin-spin interactions is to cause splitting of the order of 10^2 to 10^1 cm^{-1} , but these effects will not be considered here. However, we shall take into account the effects of covalency after the scheme of Koide and Pryce². They considered only the bonding of the e_g d-orbitals to σ ligands orbitals and defined a covalency parameter ϵ such that the amplitude of each e_g eigenfunction is diminished by the factor $(1 - \epsilon)^{\frac{1}{2}}$. Stout²³ added the first order effect due to covalency to the strong field matrices of Tanabe and Sugano and obtained the matrices as given in Table III. The parameters B_0 and C_0 are the Racah parameters for the free Mn^{2+} ion. They may be determined from the relation that $10B_0 + 5C_0 \sim 27,000$ cm^{-1} for the free Mn^{2+} ion, and also the constraint that the ratio C_0/B_0 be equal to the ratio C/B for the Racah parameters in the crystalline environment. Only half the matrix elements are listed since the matrices are symmetric. The factor $10Dq'$ in equations (7) and (8) is equal to $10Dq - 4A_0\epsilon$, where A_0 is another Racah parameter. The fitting of equations (1) through (8) to the experimental data allows one to estimate C , B , C_0 , B_0 , ϵ , $10Dq'$ and $10Dq$.

Table III: Energy Matrices in the Strong Field Representation
including the Effects of Covalency

$${}^4A_{1g}({}^4G)$$

| | |
|---|---------|
| $10B_o + 5C_o - \epsilon(10B_o + 5C_o)$ |(4) |
|---|---------|

$${}^4A_{2g}({}^4F)$$

| | |
|---|---------|
| $.22B_o + 7C_o - \epsilon(38B_o + 11C_o)$ |(5) |
|---|---------|

$${}^4E_g({}^4P, {}^4G)$$

| | | |
|---|--|---------|
| $13B_o + 5C_o$ $- \epsilon(4B_o + 2C_o)$ | $2\sqrt{3} B_o - \epsilon 2\sqrt{3} B_o$ |(6) |
| | $14B_o + 5C_o - \epsilon(22B_o + 7C_o)$ | |

$${}^4T_{1g}({}^4P, {}^4F, {}^4G)$$

| | | |
|---|---|---|
| $10B_o + 6C_o - 10Dq'$ $- \epsilon(18B_o + C_o)$ | $3\sqrt{2} B_o - \epsilon(3\sqrt{2}/2) B_o$ | $C_o - \epsilon C_o$ |
| | $19B_o + 7C_o - \epsilon(4B_o + 2C_o)$ | $10B_o + 6C_o + 10Dq'$ $- \epsilon(10C_o)$ |

....(7)

Table III: Energy Matrices in the Strong Field Representation
including the Effects of Covalency

--con't.

${}^4T_{2g} ({}^4F, {}^4G, {}^4D)$

| | | |
|--|---|---|
| $18B_0 + 6C_0 - 10Dq'$ $- \epsilon(26B_0 + C_0)$ | $\sqrt{6} B_0 - \epsilon(\sqrt{6}/2) B_0$ | $4B_0 + C_0$ $- \epsilon(4B_0 + C_0)$ |
| | $13B_0 + 5C_0 - \epsilon(4B_0 + 2C_0)$ | $18B_0 + 6C_0 + 10Dq'$ $- \epsilon(8B_0 - 10C_0)$ |

.... (8)

B. EPR Theory

a) Zeeman Interaction

An external magnetic field will interact with any unpaired electron by virtue of the electron orbital and spin magnetic moments.

The moments for a valence electron are:

$$\vec{\mu}_l = \frac{e}{2mc} \vec{P}_l, \text{ where } P_l = \hbar \sqrt{l(l+1)}$$

and

$$\vec{\mu}_s = 2 \frac{e}{2mc} \vec{P}_s, \text{ where } P_s = \hbar \sqrt{s(s+1)}$$

In these formulae, the orbital magnetic moment, $\vec{\mu}_l$, and the spin magnetic moment, $\vec{\mu}_s$, are defined in terms of the orbital angular momentum, \vec{P}_l , and the spin angular momentum, \vec{P}_s , respectively. The other quantities are e for the electron charge, m the electron mass, and c the velocity of light. In iron group elements, the electrons have their spin and orbital parts coupled by what is known as Russell-Sanders coupling. In this case, total angular momentum is defined as the vector sum of the orbital and spin angular momenta. The magnetic moment of the coupled system is defined as:

$$\vec{\mu}_j = g \frac{e}{2mc} \vec{P}_j, \text{ where } P_j = \hbar \sqrt{j(j+1)}$$

where g is the spectroscopic splitting factor.

If the electron spin were absolutely free and had no coupling to any orbital motion, the g-factor would equal the Landé g-factor for a free electron which is 2 (or, more exactly, 2.0023 with the relativistic correction). In practice the g-value varies slightly from this value for iron group elements. The orbital part of the magnetic moment is dependent on the crystal field and thus its magnitude is different for different orientations of the magnetic field H, and shows an angular variation which has the symmetry of the crystal field.

The interaction energy of the total magnetic moment $\vec{\mu}_j$ for several unpaired electrons with the external magnetic field is:

$$\begin{aligned} H_{\text{Zeeman}} &= \vec{\mu}_j \cdot \vec{H} \\ &= g \frac{e}{2mc} \vec{P}_j \cdot \vec{H} \\ &= g \frac{e}{2mc} \hbar \vec{J} \cdot \vec{H} \quad \dots(9) \end{aligned}$$

The quantity $\beta = \frac{eh}{2mc}$ is the Bohr magneton and so equation (9) can be written as:

$$H_{\text{Zeeman}} = g\beta \vec{J} \cdot \vec{H} \quad \dots(10)$$

This interaction gives rise to the fine structure of the EPR spectrum. There is also a direct interaction between the magnetic field and the nuclear magnetic moment but its magnitude is very small compared with the electronic interaction. The Zeeman interaction for Mn^{2+} results in five electronic energy levels being observed.

b) Hyperfine Structure

Since divalent manganese has an S ground state, one would not expect to observe any hyperfine structure. But all the spectra of manganese exhibit a very large hyperfine splitting. It has been supposed by Abragam and Pryce²⁴ that such splitting would result from an interaction between configurations of the type $3s 3d^n 4s$ and the $3d^n$ ground state; only a relatively small admixture would be necessary to account for the observed splitting.

The unpaired s electrons contribute to the hyperfine splitting through the Fermi contact term given by:

$$H_{H.F.} = 2\gamma\beta \beta_n \sum_k \left(\frac{8\pi}{3} \delta(r_k) \vec{s}_k \cdot \vec{I} \right) \dots (11)$$

where $\delta(r_k)$ is the Dirac δ function, γ is the nuclear gyromagnetic

ratio, β is the Bohr magneton, β_n is the nuclear magneton, r_k is the distance between the nucleus and the k 'th unpaired s electron, and the summation is over the electrons.

In addition to this, Simanek and Muller⁷ said that the origin of the manganese hyperfine splitting is due to exchange polarization of the inner $1s$, $2s$ and $3s$ orbitals. This exchange interaction sets up an attractive potential between electrons of parallel spin of the $3d$ and inner shell cores resulting in a net antiparallel polarization at the nucleus. The degree of exchange polarization is proportional to the $3d$ spin of the atom and therefore reflects $3d$ convalency.

The dipole-dipole interaction between the nucleus and the orbital motion of the electrons will in general also contribute to the hyperfine splitting. In the case of S -state ions, however, the matrix of this interaction is traceless and so the effect will average out to zero.

It is also realized that the hyperfine coupling is slightly temperature dependent because of phonon motion contributions. Orbach and Simanek²⁵ have calculated zero-point phonon contribution to the hyperfine splitting of Mn^{2+} in MgO and SrO with a cubic

crystalline environment and have shown it to be 0.97% and 1.70%, respectively, for these hosts.

The magnetic field produced at the nucleus due to the contact term quantizes the nuclear magnetic moment into $2I + 1$ different orientations. Since Mn^{2+} has a nuclear spin of $5/2$, the resulting perturbation of the electronic system of the ion splits each of the five electronic energy levels into $2I + 1 = 6$ lines. These six lines are in general unequally spaced and the spacing can be predicted from perturbation theory involving the second order approximation.

It is apparent that the hyperfine interaction involves electrons and hence its magnitude would be dependent on the electron density near the nucleus. This density is to an extent controlled by the bonding of the paramagnetic ion to the ligands and thus one might expect a relationship between the magnitude of the hyperfine splitting and the covalency, or ionicity, of the bond between the ion and the surrounding ligands. An approximate linear relation between the hyperfine splitting and amount of covalency (or ionicity) has been reported by Matumura⁵, Henning⁶, and Simanek and Muller⁷. The bonding parameter is based on Pauling's⁸ definition of electronegativity. The empirical plots indicate that there is an increase

in hyperfine splitting when the covalency decreases. This is explained by the fact that the electrons spend more time near the paramagnetic ion than near the ligands for the condition of low covalency. This increases the interaction between the ion electrons and the nucleus and gives a corresponding increase to the hyperfine splitting.

c) The Spin Hamiltonian

If it was necessary to mathematically take into account all the interactions which affect the ground state of the paramagnetic ion when describing EPR spectra, the resulting Hamiltonian would be very complicated. Included would be the Coulomb interaction, the crystal field interaction, spin-orbit coupling, spin-spin interactions, and various magnetic interactions. Fortunately, the EPR spectra can be described by a simplified Hamiltonian which accounts for the ground state energy levels between which EPR transitions occur. The formulation is called the spin Hamiltonian method. It was initially introduced by Pryce²⁶, and Abragam and Pryce²⁴. These authors first transformed the various terms in the general Hamiltonian to a form involving appropriate angular momentum operators J , L and S . The ground state was then described by an effective electron spin S' . Hence, the complicated behaviour of the

lowest energy level of the paramagnetic ion could be described in a relatively simple way involving a relatively few number of parameters. Transitions between $2S' + 1$ levels are observed in EPR experiments. The effective moment of the dipole with effective spin S' is not given by the classical Landé g -factor but by a g -factor which may differ considerably from it. In some cases, e.g., in the ${}^6S_{5/2}$ state, the fictitious spin is identical to the free spin ground state and therefore the g -value is close to the free spin g -value. Use of a particular spin Hamiltonian involves the determination by EPR studies of the symmetry of the crystal field which is operative.

The interaction terms describing the paramagnetic resonance spectra of Mn^{2+} in the spin Hamiltonian are as follows:

i) The Zeeman interaction. The Zeeman term given in equation (10) can be written for the case of an orbital singlet for measurements along the principal axis of the g tensor as

$$\begin{aligned} H_{\text{Zeeman}} &= \vec{S} \cdot \vec{g} \cdot \vec{H} \\ &= \beta g_x S_x H_x + \beta g_y S_y H_y + \beta g_z S_z H_z \end{aligned}$$

ii) The hyperfine interaction. Following Abragam and Pryce²⁴, the hyperfine interaction given by equation (11) can be written as

$$H_{H.F.} = \sum_{i,j} A_{ij} I_i S_j$$

The A_{ij} principal axes are taken to be along the g tensor axes. For an orthorhombic crystalline electric field, we can write

$$H_{H.F.} = A I_z S_z + B I_y S_y + C I_x S_x$$

iii) The crystalline electric field interaction. The spin Hamiltonian for a crystalline electric field of orthorhombic symmetry is given by Vinokurov et al²⁷, as being

$$H_{C.F.} = 1/3 b_2^0 O_2^0 + 1/3 b_2^2 O_2^2 + 1/60 b_4^0 O_4^0 + 1/60 b_4^2 O_4^2 + 1/60 b_4^4 O_4^4$$

The form of these operators is given by Orbach²⁸:

$$O_2^0 = 3S_z^2 - S(S+1)$$

$$O_2^2 = 1/2 (S_+^2 + S_-^2)$$

$$O_4^0 = 35S_z^2 - [30S(S+1) - 25] S_z^2 - 6S(S+1) + 3S^2(S+1)^2$$

$$O_4^2 = 1/4 \{ [7S_z^2 - S(S+1) - 5] (S_+^2 + S_-^2) + (S_+^2 + S_-^2) [7S_z^2 - S(S+1) - 5] \}$$

$$O_4^4 = 1/2 [S_+^4 + S_-^4]$$

where

$$S_+ = S_x + iS_y$$

$$S_- = S_x - iS_y$$

The matrix elements for these operators in various manifolds are given by Low²¹. The matrix elements of O_2^0 and O_4^0 are diagonal while those of O_2^2 , O_4^2 and O_4^4 are off-diagonal. Their values in the $S = 5/2$ manifold are:

$$O_2^0: \quad (\pm 1/2 \mid O_2^0 \mid \pm 1/2) = -8$$

$$(\pm 3/2 \mid O_2^0 \mid \pm 3/2) = -2$$

$$(\pm 5/2 \mid O_2^0 \mid \pm 5/2) = 10$$

$$O_2^2: \quad (\pm 3/2 \mid O_2^2 \mid \mp 1/2) = 3\sqrt{2}$$

$$(\pm 5/2 \mid O_2^2 \mid \pm 1/2) = \sqrt{10}$$

$$O_4^0: \quad (\pm 1/2 \quad |O_4^0| \quad \pm 1/2) = \quad 120$$

$$(\pm 3/2 \quad |O_4^0| \quad \pm 3/2) = \quad -180$$

$$(\pm 5/2 \quad |O_4^0| \quad \pm 5/2) = \quad 60$$

$$O_4^2: \quad (\pm 3/2 \quad |O_4^2| \quad \mp 1/2) = \quad -15/2$$

$$(\pm 5/2 \quad |O_4^2| \quad \pm 1/2) = \quad 9/10$$

$$O_4^4: \quad (\pm 5/2 \quad |O_4^4| \quad \mp 3/2) = \quad 12/5$$

d) EPR Transitions for Mn^{2+} in Blodite and Newberyite

The combined spin Hamiltonian for Zeeman, crystal field and hyperfine interactions is

$$\begin{aligned} H = & \beta g_x S_x H_x + \beta g_y S_y H_y + \beta g_z S_z H_z + 1/3 b_2^0 O_2^0 + 1/3 b_2^2 O_2^2 \\ & + 1/60 b_4^0 O_4^0 + 1/60 b_4^2 O_4^2 + 1/60 b_4^4 O_4^4 + A I_z S_z + B I_y S_y \\ & + C I_x S_x . \end{aligned}$$

The matrix elements of the above Hamiltonian, when the magnetic field is along the z axis, are given in the appendix. The matrix is

diagonalized to the second order of perturbation theory to obtain the energy eigenvalues. Using the selection rules; $\Delta M_S = \pm 1$, $\Delta m_I = 0$, for allowed transitions, the magnetic field positions of the hyperfine lines along the z-axis are then given by:

$$\begin{aligned}
 H_{5,1} &= H_0 \mp 4b_2^0 \mp 4b_4^0 + \frac{4}{9} \frac{(b_2^2)^2}{H_0} \\
 (\pm 5/2, m \rightarrow \pm 3/2, m) & - \frac{1}{20} \frac{(b_4^2)^2}{H_0} - \frac{b_2^2 b_4^2}{H_0} \\
 & - Am - \frac{B^2 + C^2}{4H_0} [I(I+1) - m^2]
 \end{aligned}
 \dots(12)$$

$$\begin{aligned}
 H_{4,2} &= H_0 \mp 2b_2^0 \pm 5b_4^0 - \frac{5}{9} \frac{(b_2^2)^2}{H_0} \\
 (\pm 3/2, m \rightarrow \pm 1/2, m) & - \frac{9}{80} \frac{(b_4^2)^2}{H_0} - \frac{1}{20} \frac{(b_4^4)^2}{H_0} - \frac{b_2^2 b_4^2}{2H_0} \\
 & - Am - \frac{B^2 + C^2}{4H_0} [I(I+1) - m^2] \mp \frac{BC}{H_0} m
 \end{aligned}
 \dots(13)$$

$$\begin{aligned}
 H_3 &= H_0 - \frac{8}{9} \frac{(b_2^2)^2}{H_0} + \frac{1}{10} \frac{(b_4^2)^2}{H_0} \\
 (1/2, m \rightarrow -1/2, m) &+ \frac{2b_2^2 b_4^2}{H_0} - Am - \frac{B^2 + C^2}{4H_0} \\
 &[I(I + 1) - m^2]
 \end{aligned}
 \dots (14)$$

The magnetic field positions for the EPR lines along the x and y-axes can be obtained by using the transformations of Vinokurov²⁷ et.al. as listed in Table IV. The value of A is obtained by taking the average of the hyperfine line spacings along the z-axis; parameters B and C are similarly obtained for the y and x-axes.

Knowing A, B, and C, and choosing transitions with a known m, equations (12), (13) and (14) can then be used to evaluate the g-values and the parameters b_2^0 , b_2^2 , and b_4^0 . The values obtained for b_4^2 and b_4^4 cannot be considered precise as they only have a small effect when employing second-order perturbation theory for measurements along the magnetic axis.

Table IV: Relationship between the Parameters of the Spin Hamiltonian for different orientations of the magnetic field H.

| H Z | H X | H Y |
|---------|---------------------------------|---------------------------------|
| b_2^0 | $-1/2(b_2^0 - b_2^2)$ | $-1/2(b_2^0 + b_2^2)$ |
| b_2^2 | $1/2(3b_2^0 + b_2^2)$ | $1/2(3b_2^0 - b_2^2)$ |
| b_4^0 | $1/8(3b_4^0 - b_4^2 + b_4^4)$ | $1/8(3b_4^0 + b_4^2 + b_4^4)$ |
| b_4^2 | $-1/2(5b_4^0 - b_4^2 - b_4^4)$ | $-1/2(5b_4^0 + b_4^2 - b_4^4)$ |
| b_4^4 | $1/8(35b_4^0 + 7b_4^2 + b_4^4)$ | $1/3(35b_4^0 - 7b_4^2 + b_4^4)$ |
| A | B | C |
| B | A | A |
| C | C | B |

e) S-state Zero Field Splitting.....

Zero field splitting is observed for the ground S-state which has zero orbital angular momentum and should not be directly affected by any crystalline electric field or by spin-orbit coupling interactions. Group-theoretical calculations by Bethe²⁹ indicate that in a crystal field of predominantly cubic symmetry the six-fold level will be split into one four-fold degenerate level and one two-fold degenerate level. The deviations from cubic symmetry cause a further splitting of the four-fold level into two two-fold degenerate levels. Hence, there exists three two-fold degenerate levels for the ground state zero field splitting. The mechanism by which such a splitting can occur has been discussed in many papers, but as yet no completely satisfying theory has been developed.

Van Vleck and Penney³⁰ supposed that the S-state was not pure, but had a small admixture of higher multiplets and configurations. Thus it could be split through higher order effects of the crystalline electric field, V , and spin-orbit coupling, W_{LS} .

Abragam and Pryce²⁴ suggested a mechanism, of second order, which might be responsible for the splitting of the ${}^6S_{5/2}$ level, involving the spin-spin interaction, W_{SS} , between the $3d^5$ electrons of the

paramagnetic ion. The mechanism whereby such splitting takes place can be described as follows. In each of the substates $M_S = \pm 5/2, \pm 3/2, \pm 1/2$, which correspond to the various orientations of the total spin S , the spins of the individual $3d^5$ electrons are also differently oriented. The dipole-dipole interaction between spin magnetic moments of the electrons depends on the orientation, and the total interaction energy is obtained by averaging this effect over the electron cloud distribution. When the distribution has spherical or cubic symmetry, the resultant energy is independent of orientation, and this mechanism would be inoperative. But if the symmetry is lowered, the different M_S levels will not longer have the same energy. Reversing all the spins does not alter the magnetic interaction so the states $+M_S$ and $-M_S$ remain degenerate and the Hamiltonian can be written as the sum of the squares of the spin components S_x, S_y , and S_z . This is a lower order interaction than that of Van Vleck and Penney, and may dominate it. The results from both arguments do not, however, satisfactorily account for the observed splitting.

The first detailed analysis of the ground state splitting was done by Watanabe³¹. He examined the effect of the higher order multiplets in perturbing the ground state. He maintained that the crystal field potential affected the ground state in even powers only

and, in fact, for any configuration just half-filled with electrons, there exists no effect of odd powers with regard to any of the physical quantities of the electron. There are also, however, configurations of other types allowed, such as $3d^4 4s$, and these can involve the potential V to the first power. The magnitude of this effect is very small because of the extremely large energy separation between states of such a configuration and the ground state.

Watanabe goes on to calculate the combined effects of V , W_{LS} and W_{SS} on the ground state splitting considering processes of order as high as six. But the analysis is not in complete agreement with the experimental data.

Gabriel, Johnston, and Powell³² then proceeded to criticize Watanabe's results and they performed another detailed analysis including contributions from odd powers of the potential.

Watanabe was further criticized by Leushin³³ for his g -value results. If the ground state was a pure S -state, it would have a g -value equal to that of the free spin (2.0023). Experimental data indicates otherwise and Watanabe attempted to account for this by considering the admixture of 4P -derived wave functions to be ground

state through W_{LS} . He obtained an expression for g giving a negative departure from the free spin value. The results were obtained in an approximation involving the intermediate crystal field. On the other hand, Leushin considered the crystal field on the ions to be of the same order of magnitude as the electrostatic interaction of their electrons, and he found not only the $4P$ states but also $4F$ and $4G$ states are admixed to the $6S_{5/2}$ state. This, he suggested, would also permit a positive departure for g as is found in Fe^{3+} , which also has a $3d^5$ electron configuration, and therefore a $6S_{5/2}$ ground state. Watanabe³⁴ also developed a theory of positive departure and attributed it to covalent bonding.

Another mechanism which has been proposed to explain the S-state splitting involves relativistic effects. Van Heuvelen³⁵ discusses the crystal field splitting for Mn^{2+} in tetragonal and cubic environments based on the theory of Wybourne³⁶. His calculations give a tetragonal splitting which is one-half the observed value but does have the correct sign. The theory also predicts a cubic field splitting which is only of second order but is smaller by as much as a factor of one hundred than is observed for Mn^{2+} .

Blume and Orbach³⁷ considered the axial field splitting of S-state ions in a deformed cubic host. They proposed a mechanism involving the spin-orbit admixture of the excited $4P$ state into the ground $6S$ state and the first-order matrix element of the axial and rhombic fields. Normally such terms would vanish but in this case a nonzero result is obtained because of mixing of the excited quartet states by the cubic crystalline field.

An attempt to correlate some of the more important contributions to the zero field splitting has been made by Sharma, Das and Orbach³⁸. They constructed models based on a point-multipole scheme and a covalency and overlap scheme. We shall use the point-multipole model here and attempt to compute the theoretical zero field splitting for Mn^{2+} in blodite. The splitting is calculated in terms of the parameters D and E which represent the axial and rhombic distortions of the crystal field respectively. These parameters are related to the coefficients b_m^n in the operator equivalent form of the crystalline potential in that $D = b_2^0$ and $E = 1/3 b_2^2$.

The first mechanism to consider is that of Watanabe. The contribution to the axial field splitting from this mechanism is

$$D_W = - \frac{1}{70} \frac{\zeta^2}{\Delta_{DS}} \frac{\langle r^2 \rangle^2}{(\Delta_{PS})^2} (B_2^0)^2 \dots (15)$$

where ζ is the one-electron spin-orbit coupling constant and taken to be 300 cm^{-1} , $\langle r^2 \rangle = 1.5482 a_0^2$ ($a_0 = 5.292 \times 10^{-9} \text{ cm}$), Δ_{DS} and Δ_{PS} are the energy differences between the free ion 4D and 6S states and the 4P and 6S states, respectively. The parameter B_2^0 is defined according to Sharma et al^{38 a)} as a coefficient in the spherical harmonic form of the axial field potential. All contributions to D and E which will be considered will be expressed in terms of these B_m^n coefficients. These coefficients are not the same as the b_m^n coefficients though they can be related to them.

In a cubic field, there is an additional contribution to D through the Watanabe mechanism. This is because the 4P state will not be pure but will contain admixtures from the 4F and 6G states.

Thus, we get

$$D_{WC} = -\frac{1}{70} \frac{\zeta^2}{\Delta_{DS}} \langle r^2 \rangle^2 (B_2^0)^2 \left| P_{\alpha\alpha} + \frac{4}{7} P_{\alpha\beta} \right|^2 \dots (16)$$

where

$$P_{\alpha\alpha} = \sum_{i=1}^3 \alpha_i^2 / \Delta_i$$

and

$$P_{\alpha\beta} = \sum_{i=1}^3 \alpha_i \beta_i / \Delta_i$$

The α_i , β_i , and Δ_i are listed in Table V for $10Dq = 10,000 \text{ cm}^{-1}$, and Δ_{DS} is the energy separation between the 4D and 6S states.

The α_i , β_i express the degree of admixture of the 4P and 4F states in forming the crystal field states, which are separated from the 6S state by Δ_i . Although the Δ_i values should be taken from the experimental data for a particular crystal, we will use the values in Table V from Sharma et al³⁸ rather than have to recalculate the admixture factors. It turns out, in anticipation of the optical results, that such a choice is not unreasonable. Upon putting the appropriate values of the constants into equation (16), we find

$$D_{WC} = -1.7417 (B_2^0)^2 \dots (17)$$

where B_2^0 is expressed in the units $e^2/2a_0^3$ and D_{WC} in cm^{-1} . In general, the coefficients B_m^n will be expressed in the natural units of $e^2/2a_0^{m+1}$ and the contributions to D and E in wavenumbers.

Table V: Values of α_i , β_i , γ_i , and Δ_i for the Mn^{2+} ion.
at $10Dq = 10,000 \text{ cm}^{-1}$.

| i | α_i | β_i | γ_i | $\Delta_i \text{ (cm}^{-1}\text{)}$ measured from 6S |
|-----|------------|-----------|------------|--|
| 1 | 0.637 | -0.135 | 0.759 | 18,546 |
| 2 | 0.751 | 0.334 | -0.570 | 36,001 |
| 3 | 0.176 | -0.933 | -0.314 | 45,138 |

The next mechanism considered is that of Blume and Orbach.

This yields

$$D_{BO} = (B_4^0)' [\sqrt{5}/36] \langle r^4 \rangle [L^2 P_{\alpha\gamma} (2P_{\alpha\alpha} - P_{\alpha\beta})] \dots (18)$$

and

$$E_{BO} = -B_4^2 (\sqrt{2}/6) \langle r^4 \rangle [L^2 P_{\alpha\gamma} (2P_{\alpha\alpha} - P_{\alpha\beta})] \dots (19)$$

where $\langle r^4 \rangle = 5.5126 a_0^4$ for Mn^{2+} and

$$P_{\alpha\gamma} = \sum_{i=1}^3 \alpha_i \gamma_i / \Delta_i ,$$

where γ_i is the admixture factor for the 4G level. The values necessary to calculate $P_{\alpha\gamma}$ are found in Table V. The coefficient $(B_4^0)'$ represents the unbalanced axial field and the coefficient B_4^2 represents the four-order rhombic field. Equations (18) and (19) reduce to

$$D_{BO} = 4.3404 (B_4^0)' \dots (20)$$

and

$$E_{BO} = -16.47275 (B_4^2) \dots (21)$$

There is also a contribution due to configurational mixing,

known as the Orbach, Das and Sharma mechanism. Calculations show it to be

$$D_{\text{ODS}} = 2.1044 (B_2^0)^2 \quad \dots (22)$$

There is no contribution to E because it is found that such a contribution is about equal, though opposite in sign, to a contribution to E from the Watanabe mechanism. Thus, both are neglected as they would cancel each other out.

The last mechanism to consider is the spin-spin mechanism of Pryce. This gives

$$D_{\text{SS}} = -0.07306 B_2^0 \quad \dots (23)$$

and

$$E_{\text{SS}} = -0.09269 B_2^2 \quad \dots (24)$$

In order to evaluate the various contributions to D and E, the coefficients B_m^n must be computed. Consider external point charges $q_j|e|$ situated at (R_j, ξ_j, ϕ_j) with respect to an origin taken at the site of the paramagnetic ion, then we get:

$$B_2^0 = \sum_j q_j (3 \cos^2 \xi_j - 1)/R_j^3 \quad \dots (25)$$

UNIVERSITY LIBRARY

$$B_2^2 = \sqrt{3}/2 \sum_j q_j \sin^2 \xi_j \cos 2\phi_j / R_j^3 \quad \dots (26)$$

$$B_4^2 = 1/2/10 \sum_j q_j (\sin^2 \xi_j) (7 \cos^2 \xi_j - 1) \cos 2\phi_j / R_j^5 \quad \dots (27)$$

$$(B_4^0)_c = 1/4 \sum_j q_j (35 \cos^4 \xi_j - 30 \cos^2 \xi_j + 3) / R_j^5 \quad \dots (28)$$

$$(B_4^4)_c = \left(\frac{35}{32}\right)^{1/2} \sum_j q_j \sin^4 \xi_j \cos^4 \phi_j / R_j^5 \quad \dots (29)$$

$$\alpha = (B_4^0)_c / (B_4^4)_c \quad \dots (30)$$

$$(B_4^0)_{nc} = 1/4 \sum_j q_j (35 \cos^4 \xi_j - 30 \cos^2 \xi_j + 3) / R_j^5 \quad \dots (31)$$

$$(B_4^4)_{nc} = 1/8/70 \sum_j q_j \sin^4 \xi_j \cos 4\phi_j / R_j^5 \quad \dots (32)$$

$$(B_4^0)' = (B_4^0)_{nc} - \alpha (B_4^4)_{nc} \quad \dots (33)$$

where c stands for the cubic environment and nc designates the non-cubic environment. If, in blodite, we consider the thirty nearest

lattice points to the Mn^{2+} site assuming two units of positive charge on the Mn^{2+} and two units of negative charge on all the lattice points, we can evaluate the crystal field potential components B_m^n . The values are listed in Table VI.

Using the values of B_m^n in equations (15), (17), (20), (21), (22), (23), and (24), we can compute the various contributions to D and E. These are listed in Table VII. We have anticipated the EPR results and listed the experimental values for D and E. The agreement is not accurate, as would be expected from some of the assumptions we have made. The theoretical value for E is considerably closer to its experimental value than that for D. This could be in part due to the imprecision in the value of B_2^0 as compared to the value of B_4^2 , which contributes greatly to E. B_4^2 converges much more rapidly than B_2^0 . More elaborate lattice summation schemes need to be used to obtain the best values for the B_m^n .

In any case, we can see the relative magnitudes of the various contributions to D and E from different mechanisms. The sign of D for its experimental value is not known and the theory would lead us to believe that it should be negative.

Table VI: Crystal Field Potential Components B_m^n
(in units of $e^2/2a_0^{m+1}$)

| | |
|------------|----------|
| B_2^0 | 0.09622 |
| B_2^2 | 0.12680 |
| B_4^2 | -0.00126 |
| $(B_4^0)'$ | -0.00189 |

Table VII: Contributions to D and E from various mechanisms
(in 10^4 cm^{-1})

| | |
|----------------|-------|
| D_W | -124. |
| D_{WC} | -161. |
| D_{BO} | -82. |
| D_{ODS} | 195. |
| D_{SS} | -71. |
| E_{BO} | 207. |
| E_{SS} | -118. |
| TOTAL D THEORY | -242. |
| TOTAL D EXP. | 334. |
| TOTAL E THEORY | 90. |
| TOTAL E EXP. | 87. |

Chapter IV

Equipment

The Spectrometer used was of commercial design and was manufactured by Hilger and Watts Ltd. It employed an eight inch Newport magnet. The spectrometer was operated at X-band (9.2 GHz) and room temperature. A rectangular cavity operating in the TE_{012} mode was used in the experiments. The magnetic field was modulated at 100 kHz.

A. Operating Principles of X-band Spectrometer

The microwave source, which is a reflex klystron, supplies about 35 mW of power, the frequency of which was locked to a reference cavity by means of an automatic frequency control (AFC) unit. The power from the klystron is split equally by a hybrid-tee junction into two side arms, one going to the sample cavity and the other carrying components which reflect back a reference wave, adjustable in phase and amplitude. The two signals are balanced so that zero or low power needed to bias the crystals detector, is detected in the fourth arm of the tee. The AFC unit operates such that a correction voltage

proportional to the frequency difference between the reference transmission cavity and the klystron is applied to the klystron, locking it to one frequency. The block diagram of this section of the spectrometer is shown in Figure 4.

The microwave signal then goes to a hybrid tee junction such that the signal is split between the cavity containing the sample and a balance arm. When the magnetic field is such that the resonance condition is satisfied, the complex magnetic susceptibility of the sample is altered. This causes the reflection coefficient of the cavity to be altered and the hybrid tee bridge becomes unbalanced. In actual practice, however, the bridge is set off-balance to begin with since the best signal-to-noise ratio for the crystal detector is obtained by working higher up the slope of the crystal characteristic. This preliminary unbalancing reflects back a small signal so that when the EPR signal is obtained, the crystal is working at the optimum slope of its characteristic. Also, if the bridge is completely balanced at first, then one will detect changes in both the real and imaginary parts of the complex susceptibility. By off-balancing the bridge, one can distinguish between the components such that off-balancing in amplitude alone allows one to detect the imaginary part of the susceptibility, a change in which gives

rise to pure absorption, while off-balancing in phase allows one to only detect the real part of the susceptibility, which signifies a change in the dispersion.

The out-of-balance signal passes through a low-noise pre-amplifier and a narrow band amplifier to a phase sensitive detector (PSD). The PSD is also fed with a reference signal from the 100 kHz oscillator. The 100 kHz oscillator also modulates the magnetic field. The phase sensitive detection system works as follows. The reference signal is used to lock a tuned amplifier to the signal frequency and phase thereby permitting a narrow band pass and hence eliminating noise. In the balanced mixer part of the PSD, the input of signal plus noise beats against the reference signal. This mixing results in an output signal described by the expression $f_o(t) = f(t) \cos \delta$, where $f(t)$ is the input and δ is the phase angle between the input and the reference. Thus the output is maximum when the phase angle is zero and minimum when it is 90° . When the signal and reference are in phase, a large portion of the total noise will be removed by the cosine factor. The output may now be filtered to smooth out additional noise, and amplified in the D.C. amplifier if necessary. The important point to note is that the output voltage of the PSD is directly proportional to the amplitude of the input signal. If the

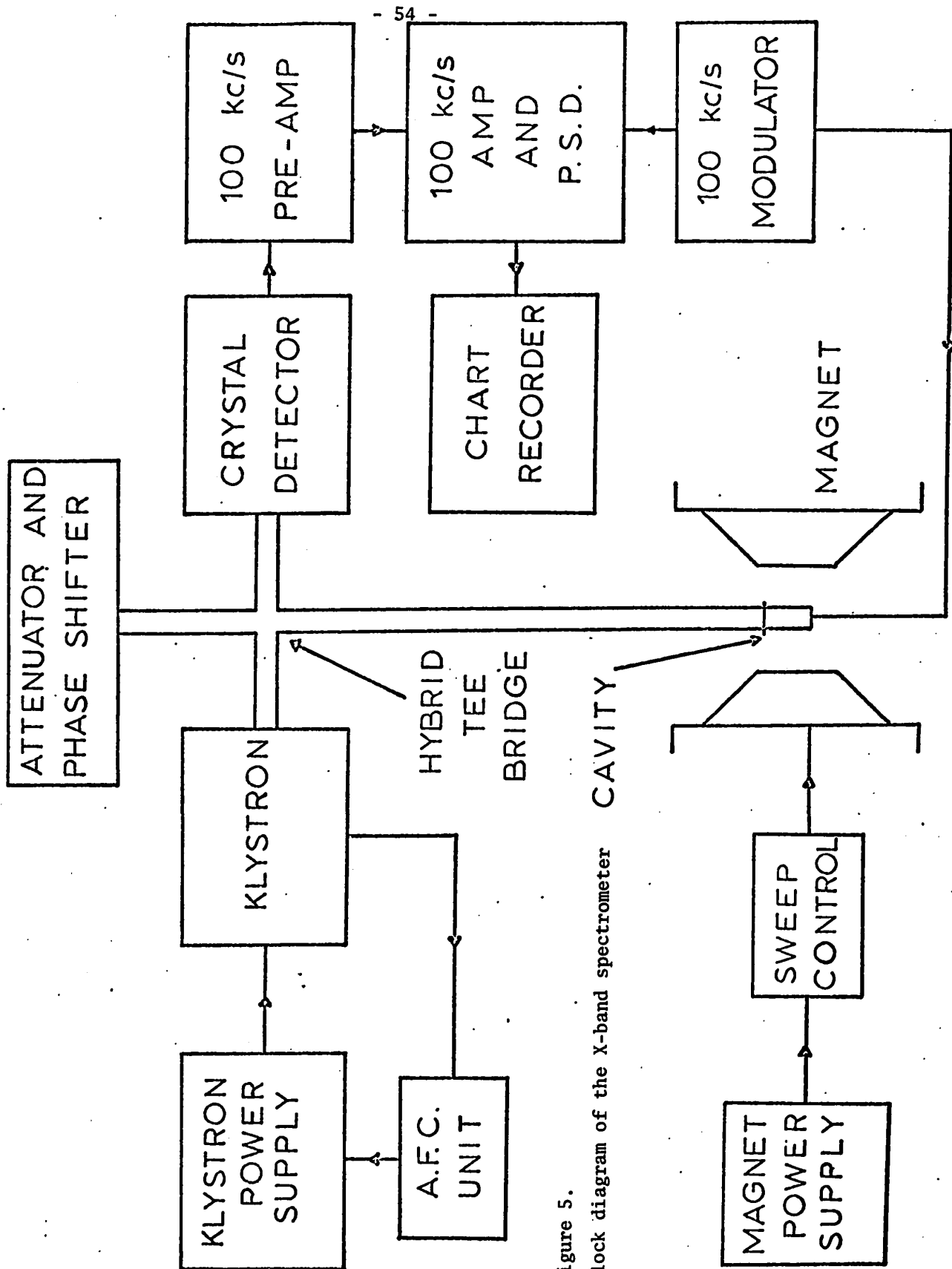


Figure 5.
Block diagram of the X-band spectrometer

modulation amplitude is kept small enough so as not to distort the output, then the output will be a true representation of the first derivative of the absorption line.

The magnet produces fields up to 15 kg and the stability is achieved by current regulation. The magnet sweep was fairly linear in the experimental range.

The block diagram for the spectrometer is shown in Figure 5.

B. X-band cavity

The cavity (Figure 6) was a rectangular reflection type operating in the TE_{012} mode. The cavity had a Q-factor of about 3,000. The sample was glued to a perspex pin and was positioned in the cavity in a region of maximum microwave r.f. magnetic field so as to maximize the signal-to-noise ratio of the resonance signals. This ratio is proportional to the square of the r.f. field signal. At the same time, the sample is placed in a position of minimum electric field so as to minimize the dielectric power loss, which reduces the signal-to-noise ratio.

UNIVERSITY LIBRARY

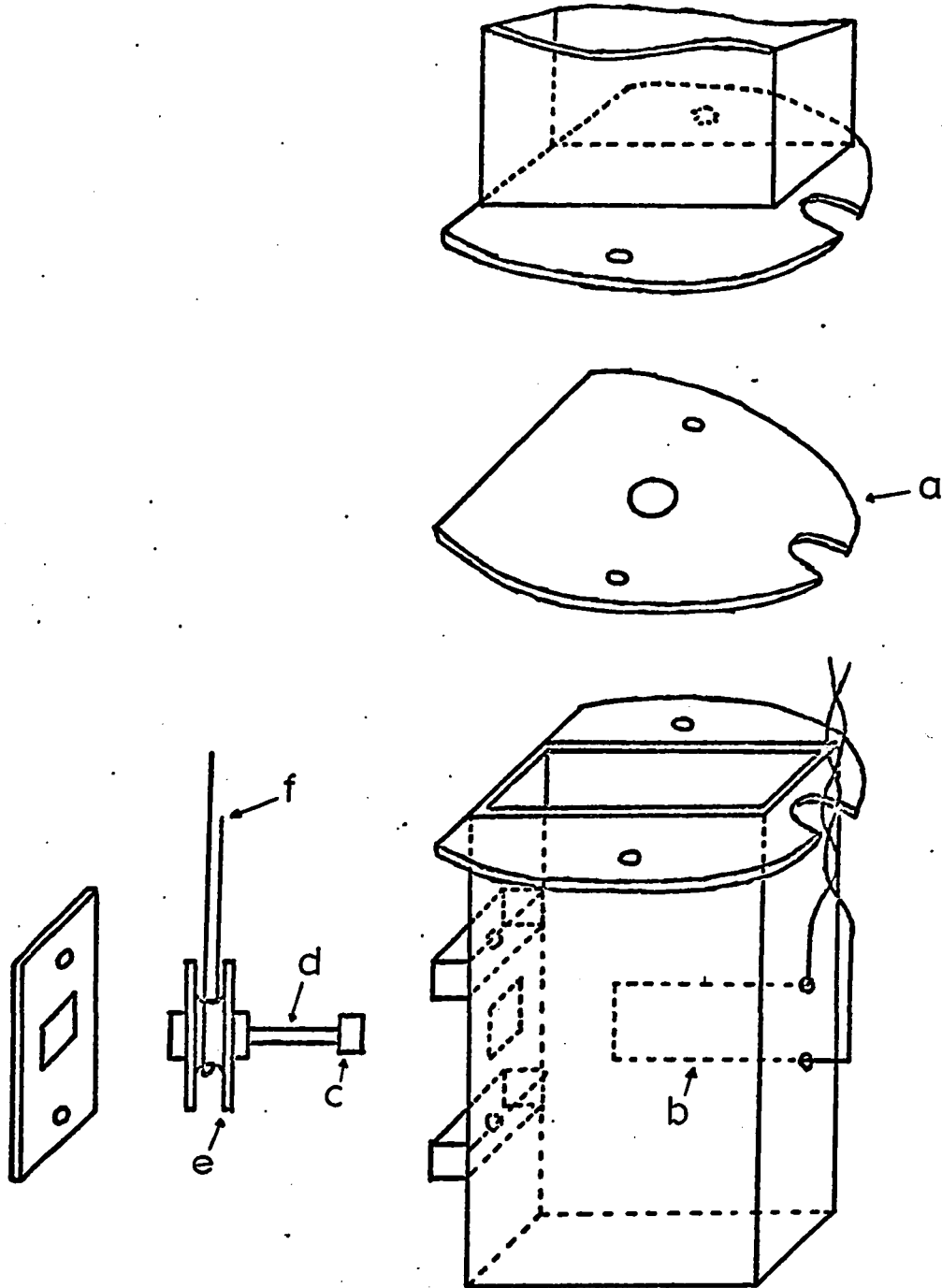


Figure 6. X-band cavity a) iris, b) modulation coil, c) sample, d) perspex pin e) lower pulley, f) string.

The magnetic field modulation was achieved by placing a half turn of wire in the shape of a hairpin at the center of the cavity, surrounding the crystal. The coil was connected to the 100 kHz oscillator. The sample pin was fastened to a pulley arrangement and so the sample could be rotated about a horizontal axis. The lower pulley contained the shaft for the sample pin and the upper pulley consisted of a calibrated dial so that the angle about the horizontal axis could be ascertained. Since the magnetic field could be rotated about a vertical axis, this arrangement allowed one to point the magnetic field in any direction in the crystal. The principal magnetic axes, which can be determined by suitable adjustments of both angles, are defined as positions of maximum separation of the resonance lines. The axes are then plotted on a stereogram.

The sample is mounted in the cavity on a pin with a reference mark. The reference mark allows one to relate the magnetic axes and the crystallographic axes. The sample can be transferred to an X-ray goniometer to determine the positions of the crystallographic axes. The correlation between the two sets of axes can be done in a simple and unambiguous way if the coordinate angles of the stereogram are correctly labelled. The labelling is determined by the way in which the crystal is aligned in the cavity and on the X-ray goniometer,

by virtue of the alignment markings on the crystal pin. The process has been described by Manoogian³⁹.

C. Magnetic Field Measurements

The magnetic field was measured by proton nuclear magnetic resonance (NMR). The proton source was a vial of water which was doped with copper sulfate. The magnetic field was modulated at 60 Hz for observation of the proton resonance, and the signal was monitored on an oscilloscope. To affect the monitoring, the horizontal input of the oscilloscope was connected to a 60 Hz source and phase shifter. The frequency at which proton resonance occurred was measured by a frequency counter. The strength of the magnetic field is obtained from the expression.

$$H \text{ (k gauss)} = \frac{\nu \text{ (MHz)}}{4.25759}$$

where ν is the proton resonance, and the quantity 4.25759 is the frequency for proton resonance in a 1 kgauss magnetic field.

D. Optical Spectrometer

A block diagram of the optical equipment is shown in Figure 7. The source is a tungsten filament. Light comes from the source through a slit arrangement into a Bausch and Lomb monochromator. The monochromator has an automatic drive for continuous change of wavelength. The monochromator light emerges from the monochromator and goes through another slit arrangement and into a black box. A lens in the box focuses the light on the sample. The transmitted light is detected in a 6255S phototube which is powered by a Keithley regulated high voltage supply. The output from the phototube is recorded on a chart recorder. The resolution of the spectrometer is about 10 \AA and the wavelength is accurate to about 25 \AA , both conditions being well within the limits for observation of optical transitions of interest here.

E. Optical Measurements

With the sample in the black box, a recording is taken of the transmitted intensity, I , as a function of wavelength. The experiment is repeated without the sample to obtain a recording of the incident intensity I_0 . The absorbance is calculated from the formula

$$A = \log_{10} \frac{I_0}{I} .$$

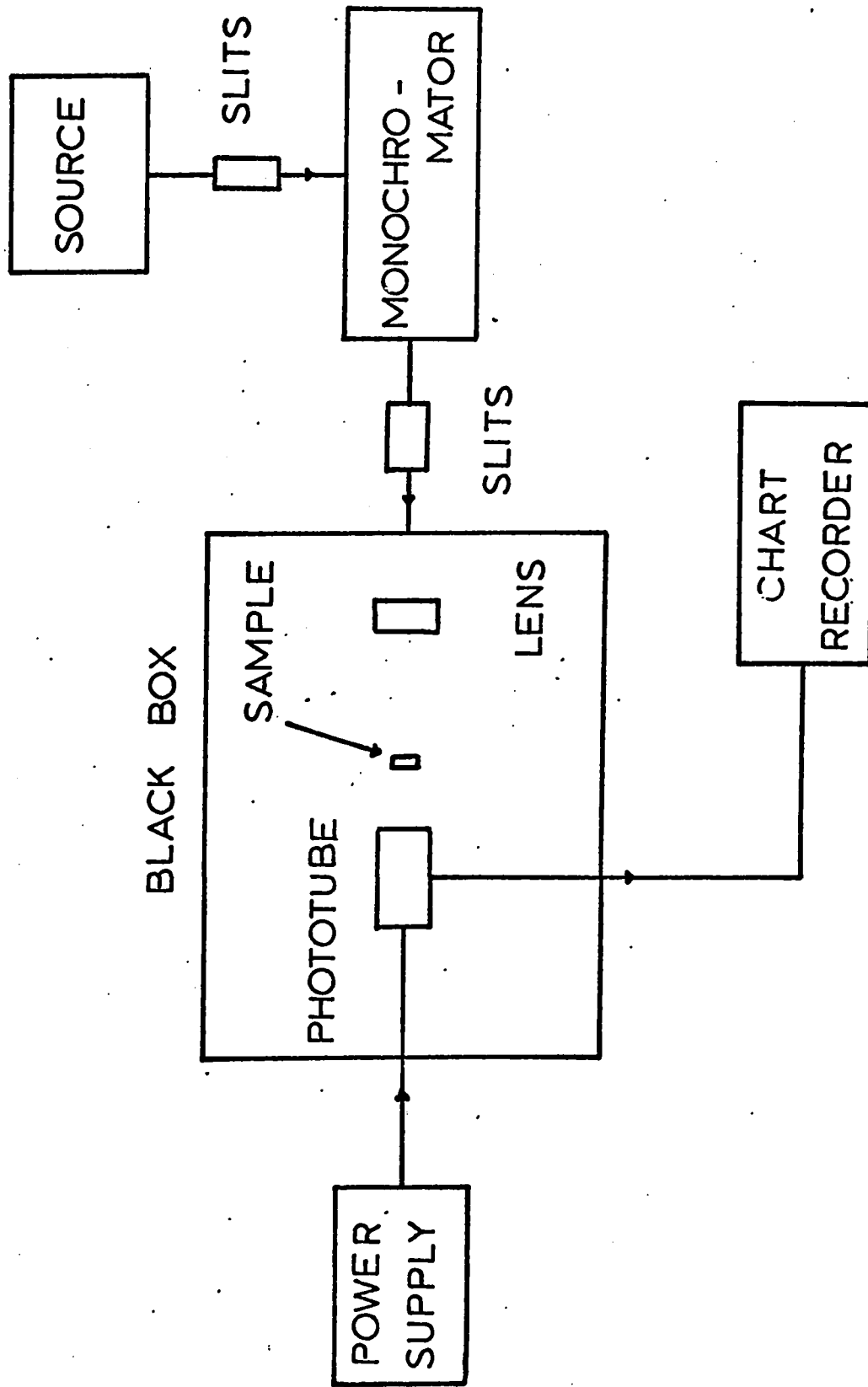


Figure 7. Block diagram of the optical absorption apparatus

A graph of absorbance versus wavelength is then plotted. The graph may be redrawn to a straight base line by estimating an appropriate exponential base line for the original absorbance spectrum. .

Chapter V

Experimental Procedure and Results

A. EPR of Blodite

Two identical, but differently oriented, magnetic complexes of Mn^{2+} were found in blodite. The magnetic complexes exhibit rhombic symmetry, with the two z axes making an angle of 100° to each other. The complexes are related by a two-fold symmetry about the crystallographic b axis, but none of the magnetic axes are constrained along the b direction. The angular relationship between the magnetic and crystallographic axes are given in the stereogram of Figure 8. From the stereogram, one can obtain the angles between the axes, and these are given in Table VIII.

The magnetic axes are defined when the five groups of six hyperfine lines of manganese in a given complex show extrema in their separations as a function of the magnetic field strength. This occurs when the external magnetic field is directed along the three perpendicular axes of the crystal field tensor. The z axis is defined as

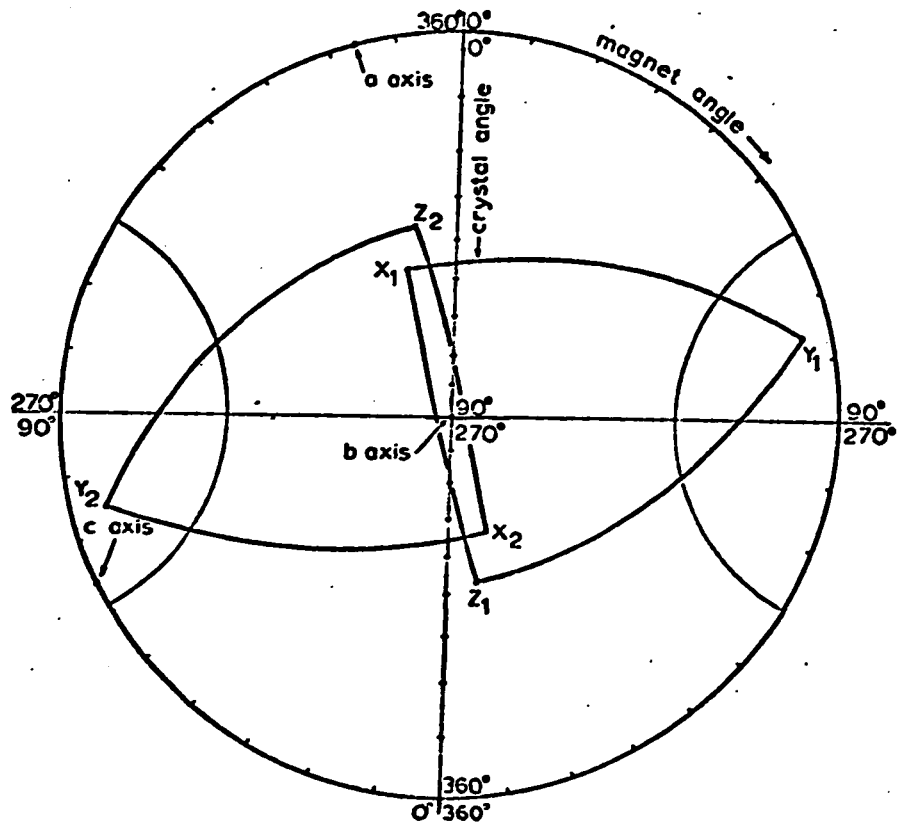


Figure 8. Stereogram showing the relationship between the Mn^{2+} magnetic axis and the crystalline axis for blodite.

Table VIII: Angular Relationships between the Magnetic and Crystallographic Axes of Mn^{2+} in Blodite (accuracy $\pm 2^\circ$)

| Axes | a | b | c | X_2 | Y_2 | Z_2 |
|-------|-------------|------------|-------------|------------|-------------|-------------|
| a | | | | 50° | 88° | 140° |
| b | | | | 40° | 85° | 55° |
| c | | | | 92° | 170° | 80° |
| X_1 | 130° | 40° | 88° | 80° | | |
| Y_1 | 92° | 85° | 10° | | 170° | |
| Z_1 | 40° | 50° | 100° | | | 100° |

UNIVERSITY MICROFILMS

the direction of greatest separation of the hyperfine groups of lines. The y axis is 90° to the z-axis and the groups of lines have a smaller separation in this direction. The x axis is mutually perpendicular to the y and z axes and the groups show an even smaller separation in this direction. A typical spectrum obtained on a chart recorder for the magnetic field along the z axis of one of the complexes is given in Figure 9. The angular variation of the lines for one complex, between the z and y magnetic axes, is given in Figure 10. In Figure 9, one can see that the central groups of six hyperfine lines is mixed with the lines of the other manganese complex, and hence there is some difficulty in obtaining accurate magnetic field measurements for the central six lines. The mixture of lines of a given complex also occurs when the magnetic field direction is displaced from the magnetic axes as shown in Figure 10. Hence, it was impossible to identify the lines of a given complex when the magnet was displaced from the z or y axes by more than 30° . This was further complicated by the appearance of forbidden lines. As seen in Figure 9, forbidden transitions appear with the second and fourth groups of hyperfine lines. These forbidden lines grow in intensity when the magnetic field is rotated from the magnetic axis. They show excellent resolution, but unfortunately it is not feasible to study their angular variation in intensity or position since the forbidden lines become mixed together

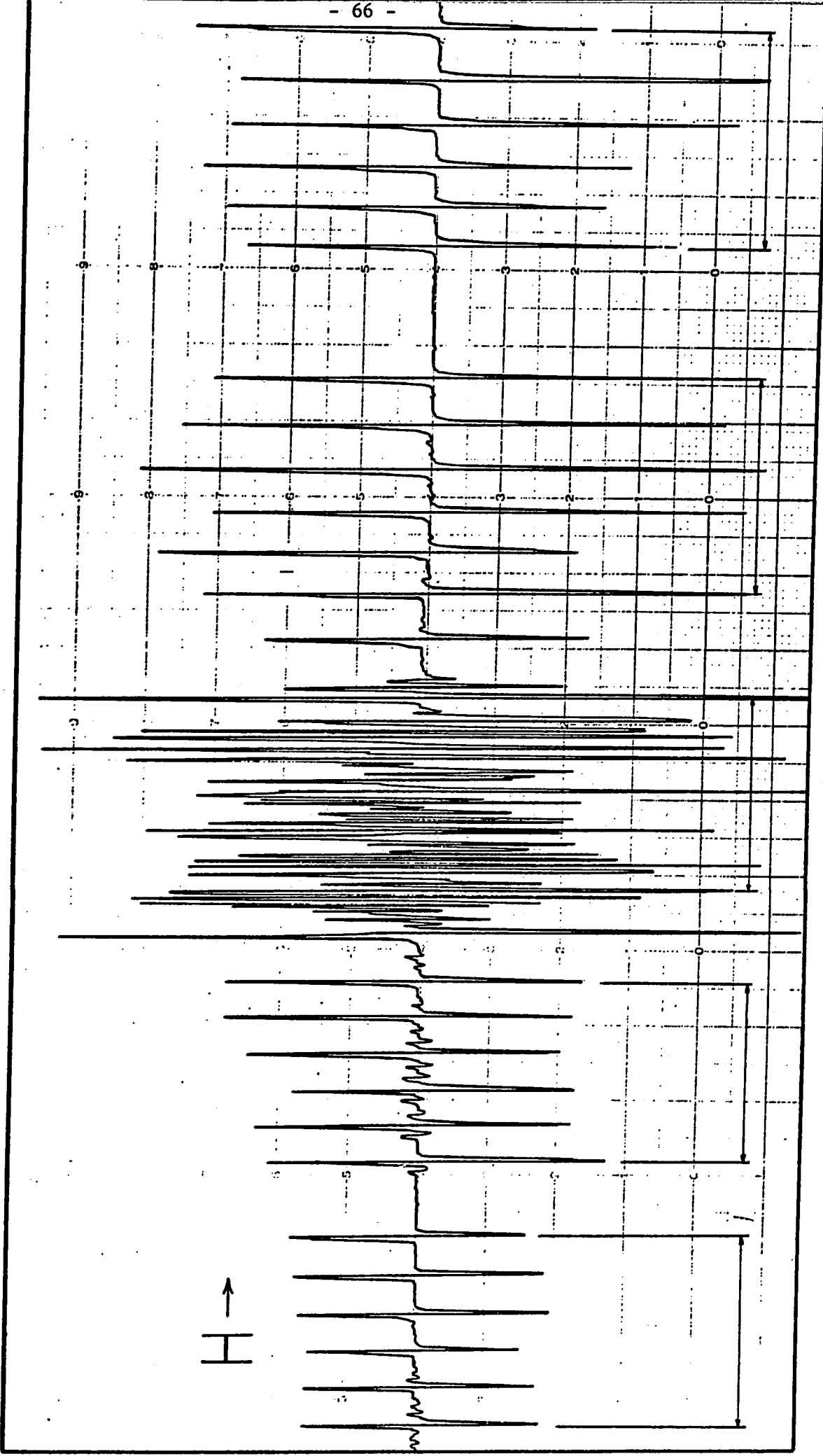


Figure 9. The spectrum of Mn²⁺ in blodite along a magnetic z axis.

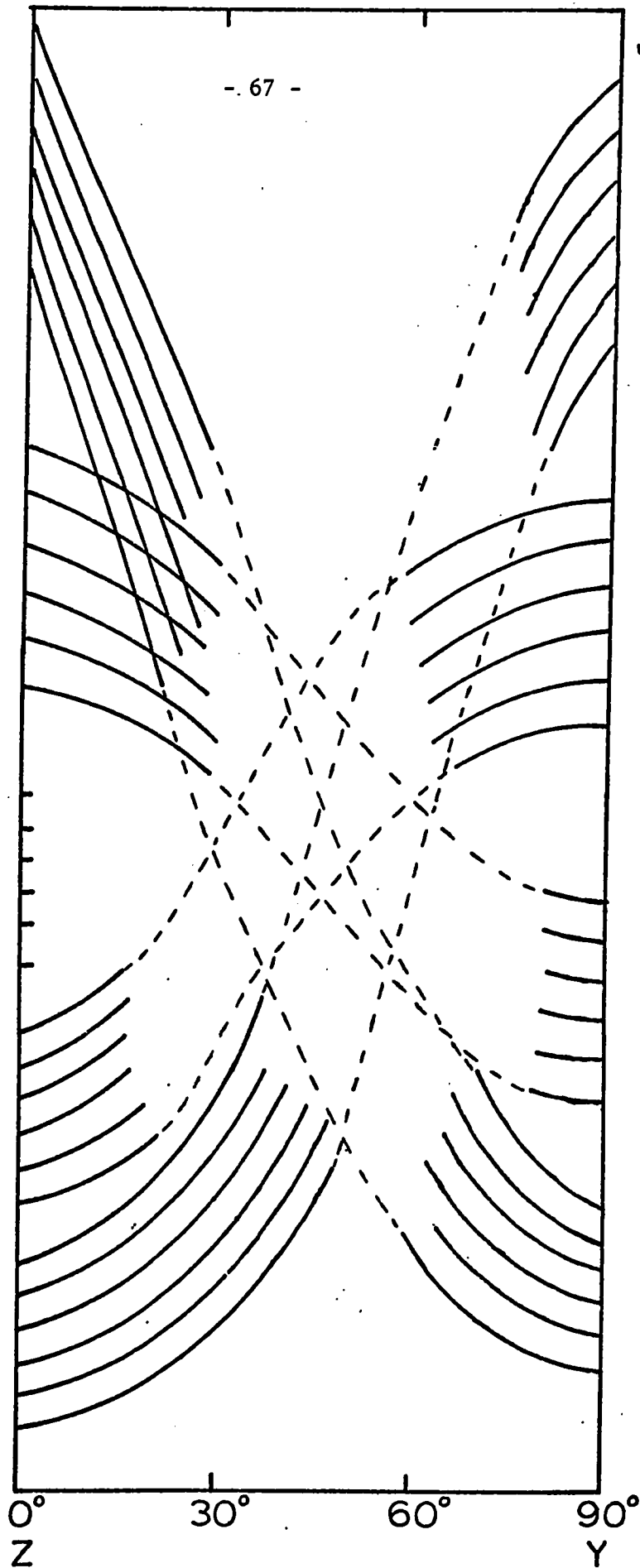


Figure 10. Angular variation in position of Mn^{2+} hyperfine lines in blodite as magnet is rotated from a z to a y magnetic axis.

in the two complexes near the y axis. This is because the y axis of the two complexes are only 10° apart.

Magnetic field measurements were made for allowed lines along the z and y magnetic axes. No measurements could be made along the x axis since the lines are all mixed together and the various transitions cannot be distinguished. The magnetic field positions for the lowest line of each hyperfine group are given in Table IX.

The results were fitted to a spin Hamiltonian of orthorhombic symmetry. The spin Hamiltonian parameters were obtained from equations (12), (13) and (14) using the information in Table IX. These are listed in Table X. The matrix of the spin Hamiltonian was constructed using the determined values of the parameters and then diagonalized to give the energy levels as a function of magnetic field strength. Energy level diagrams for the z, y, and predicted x magnetic axes were drawn and are given in Figures 11, 12, and 13. The transitions for X-band are shown in the diagrams for the centers of gravity of the groups of hyperfine lines. The reason that no measurements could be made along the x axis is shown by the closeness of the transitions in Figure 13. The complete energy level diagram including the hyperfine effects for a z direction at low field is shown in Figure 14.

Table IX: Magnetic Field Positions of the Lowest EPR Lines
for each of the Hyperfine Groups of Mn^{2+} in Blodite
(in gauss) $\nu = 9.57 \text{ GHz}$ -

| | Z axis | Y axis |
|-------|--------|--------|
| H_1 | 1,740 | 1,833 |
| H_2 | 2,453 | 2,446 |
| H_3 | 3,162 | 3,042 |
| H_4 | 3,881 | 3,682 |
| H_5 | 4,631 | 4,364 |

Table X: Spin Hamiltonian Parameters of Mn^{2+} in Blodite

| Parameter | Value |
|-----------|--|
| g | 1.993 0.0005 |
| b_2^0 | $334.0 \pm 1.5 \times 10^{-4} \text{ cm}^{-1}$ |
| b_2^2 | $260.0 \pm 1.5 \times 10^{-4} \text{ cm}^{-1}$ |
| b_4^0 | $1.2 \pm 0.2 \times 10^{-4} \text{ cm}^{-1}$ |
| A | $89.0 \pm 1.0 \times 10^{-4} \text{ cm}^{-1}$ |
| B | $86.4 \pm 0.5 \times 10^{-4} \text{ cm}^{-1}$ |

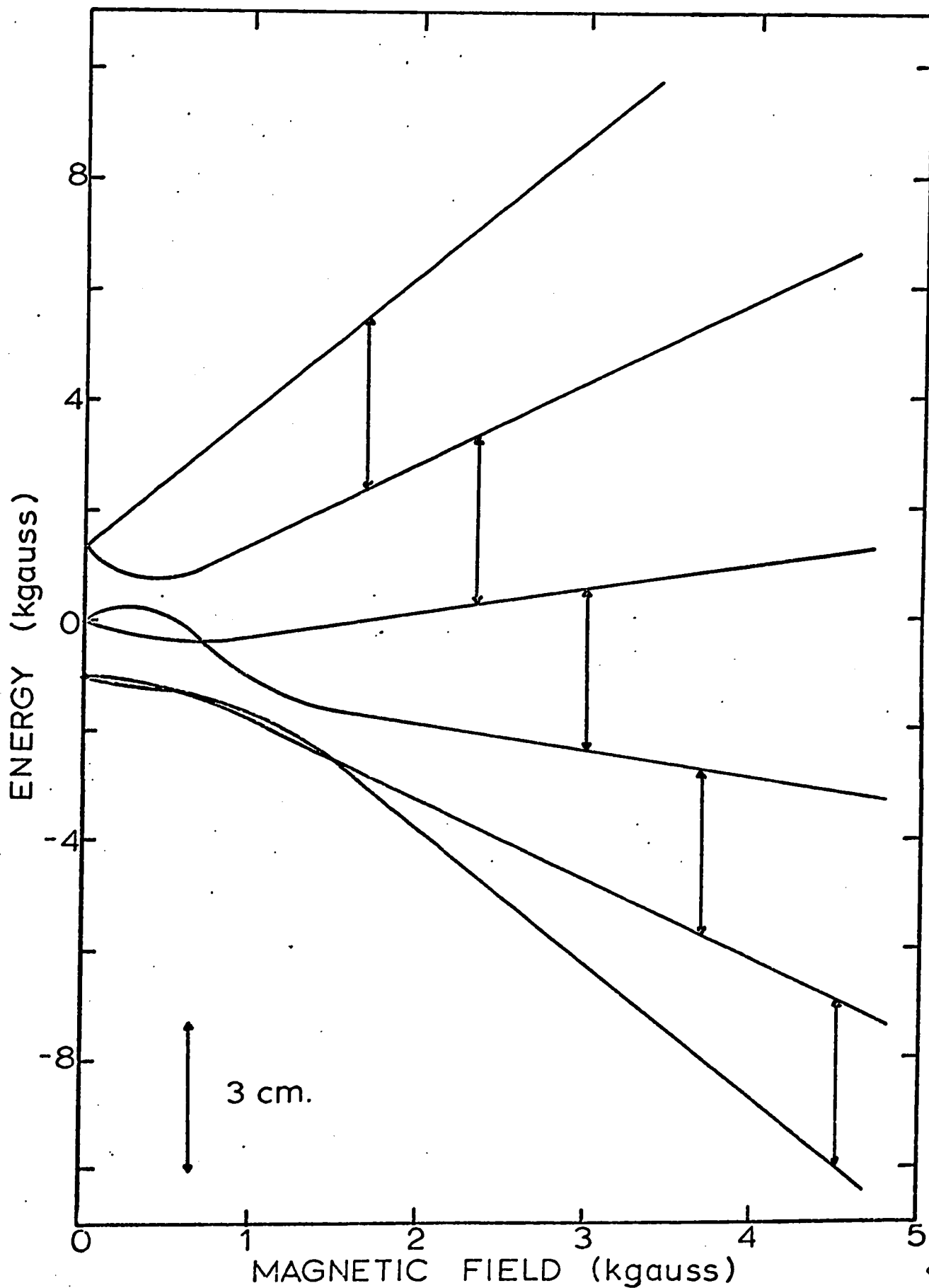


Figure 11. Energy level diagram of Mn²⁺ in blodite along a magnetic axis

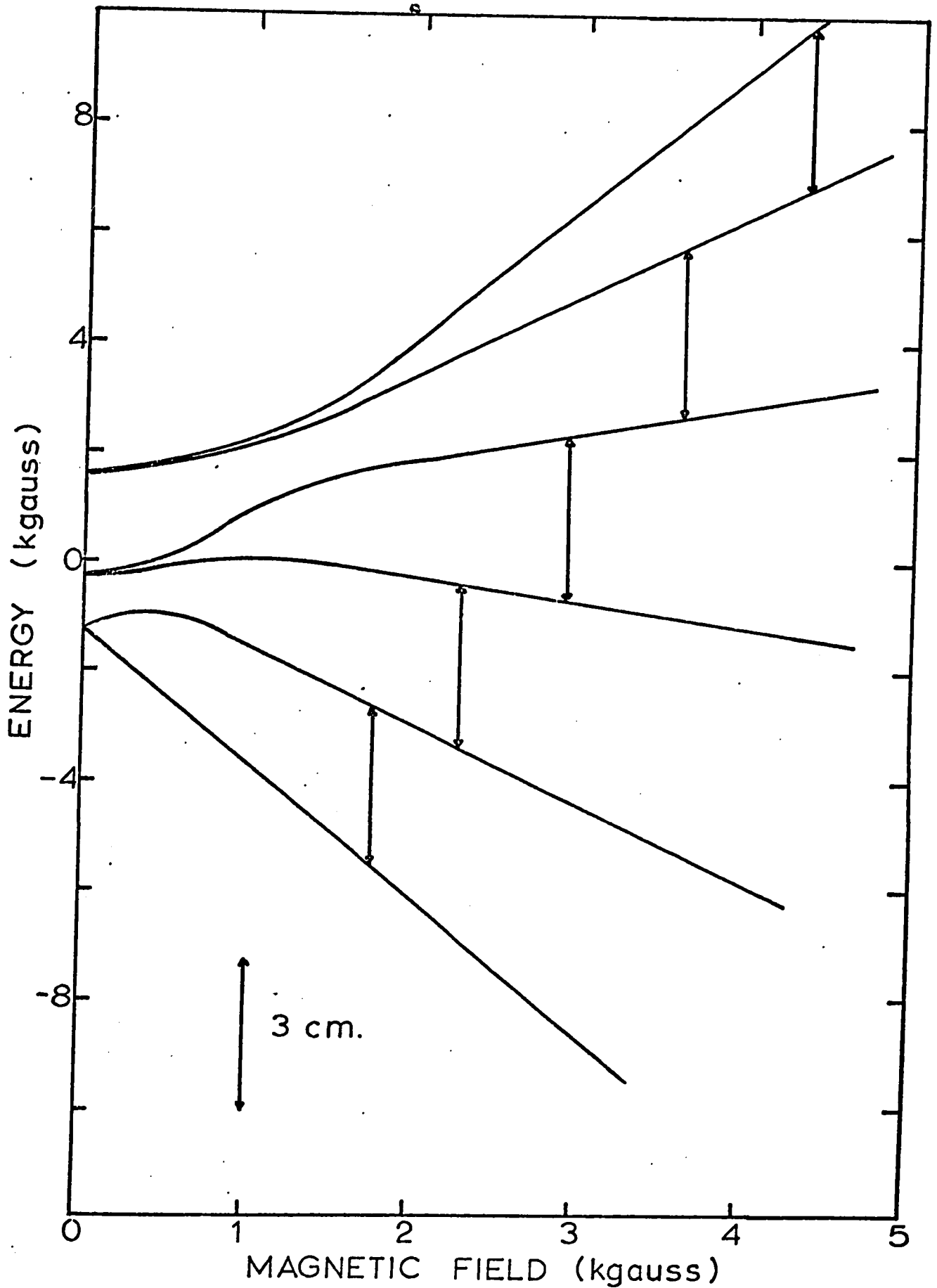


Figure 12. Energy level diagram of Mn²⁺ in blodite along a magnetic y axis.

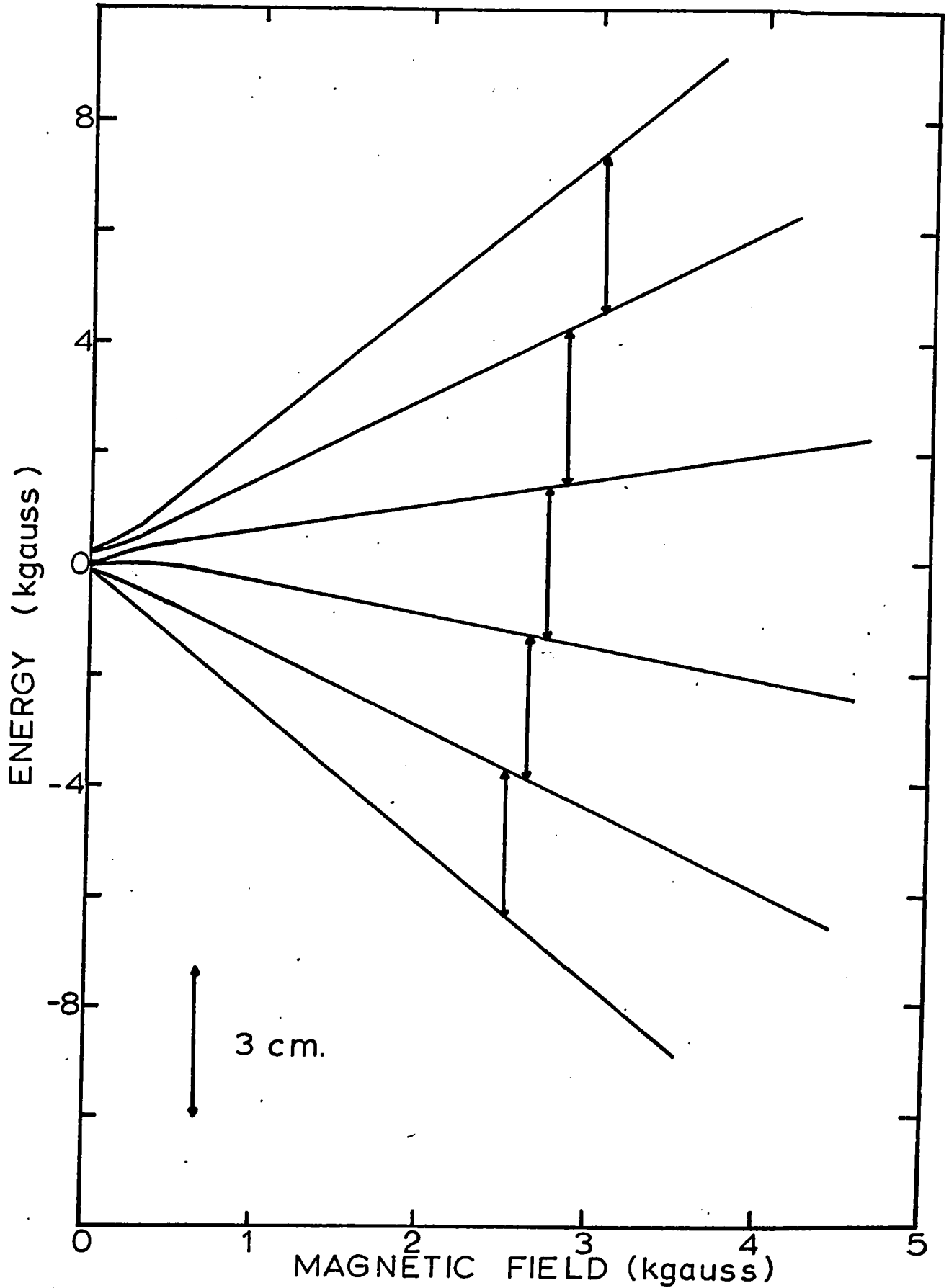


Figure 13. Energy level diagram of Mn^{2+} in blodite along a magnetic x axis.

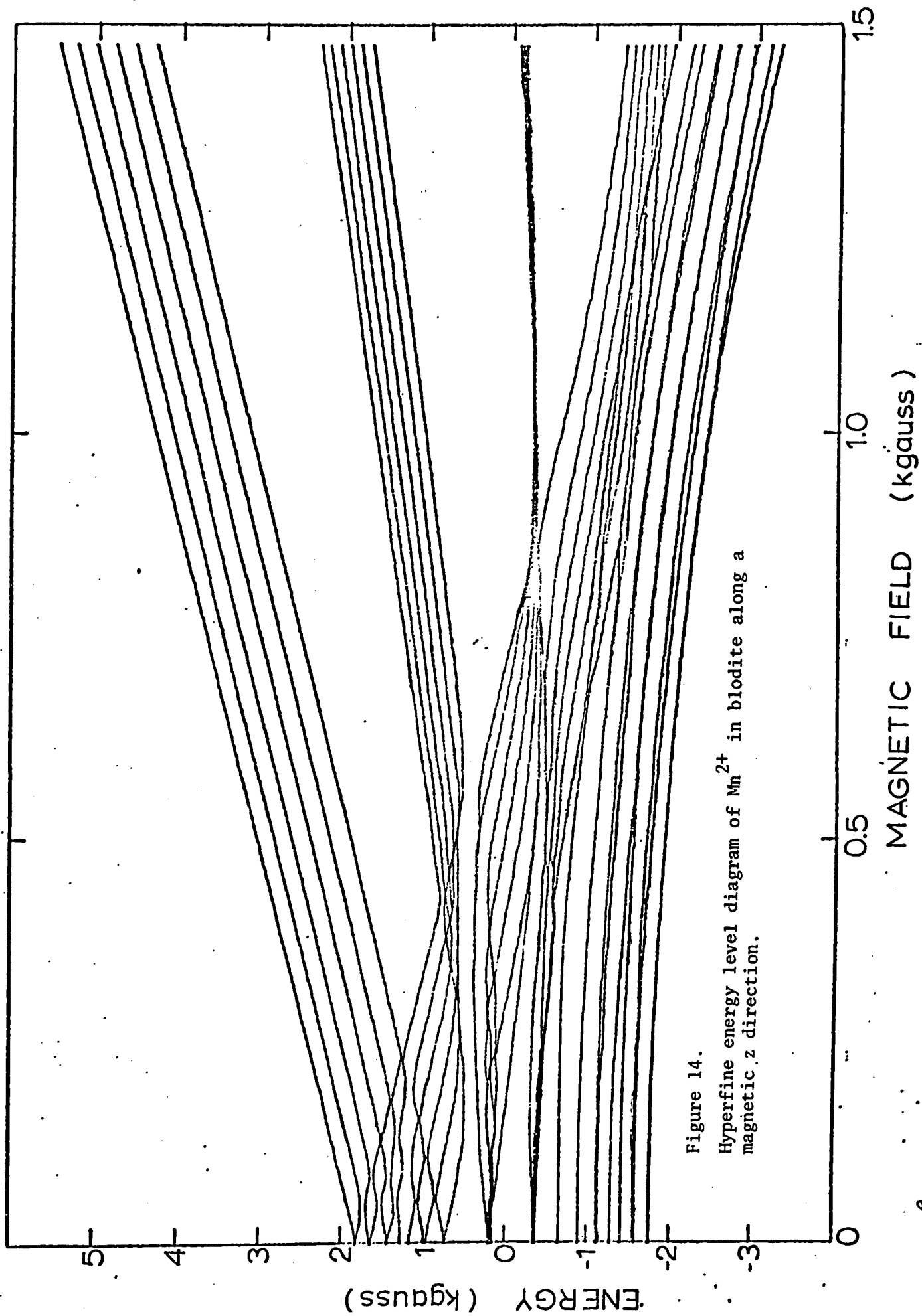


Figure 14.
Hyperfine energy level diagram of Mn^{2+} in blodite along a magnetic z direction.

B. EPR of Newberyite

The results of Mn^{2+} in newberyite were obtained in an analogous way to those obtained for Mn^{2+} in blodite. A typical spectrum of Mn^{2+} in newberyite along a z magnetic axis is given in Figure 15. For comparison purposes, we have given in Figure 16 a chart recording of the spectral lines for a z magnetic axis of Mn^{2+} in struvite.

In newberyite, two identical, but differently oriented, magnetic complexes of Mn^{2+} were found. The complexes exhibit rhombic symmetry, with the two z axes making an angle of 120° to each other. The complexes are related to each other by two-fold symmetry with respect to the crystallographic b axis. These results are given in the stereogram of Figure 17. From the stereogram we obtained the angles between the axes, and these are given in Table XI.

Magnetic field measurements were made along the y and z magnetic directions and, as in blodite, the x axis transitions were again too close to separate and identify. The magnetic field positions for the lowest line of each hyperfine group are given in Table XII.

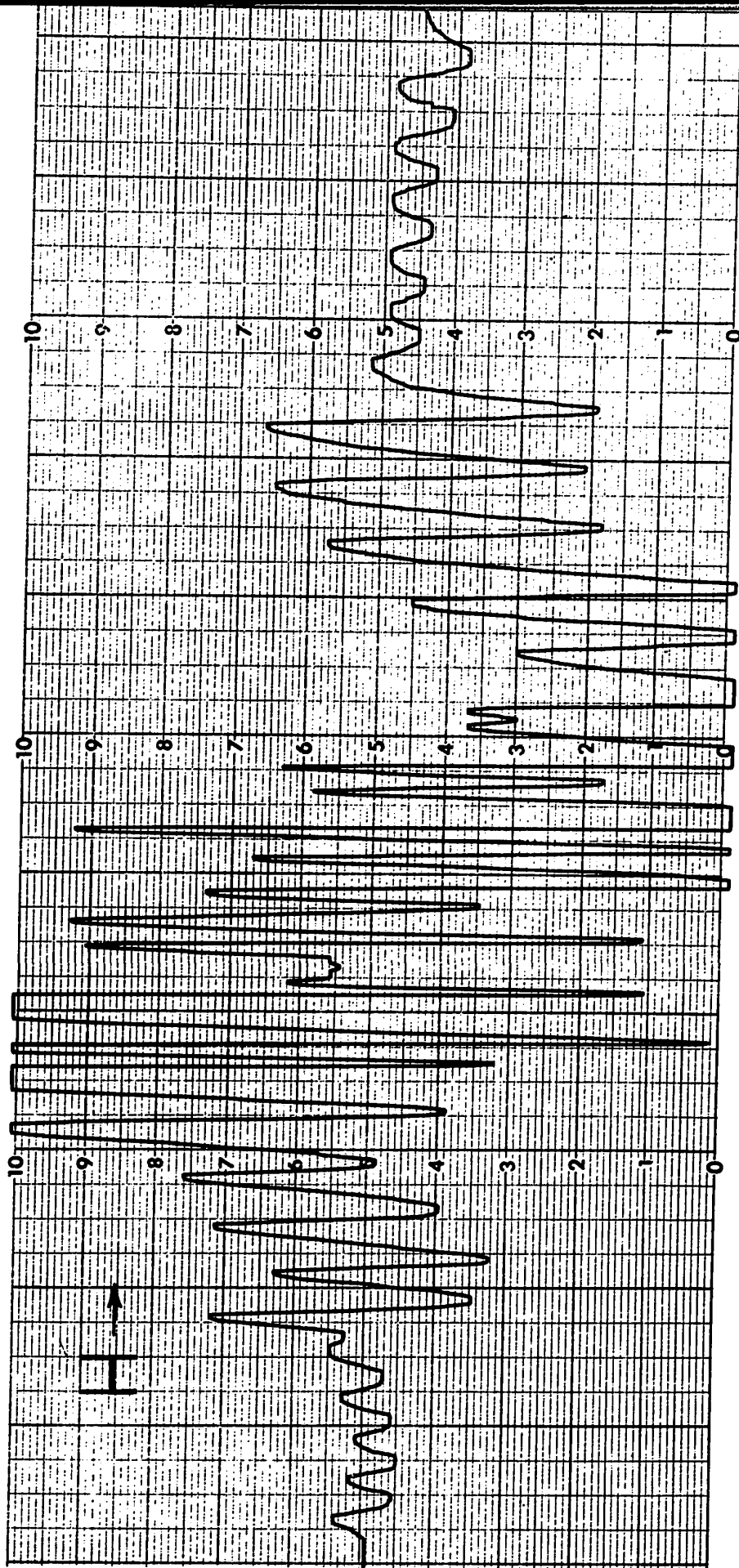


Figure 15. Spectrum of Mn^{2+} in newberyite along a magnetic z direction.

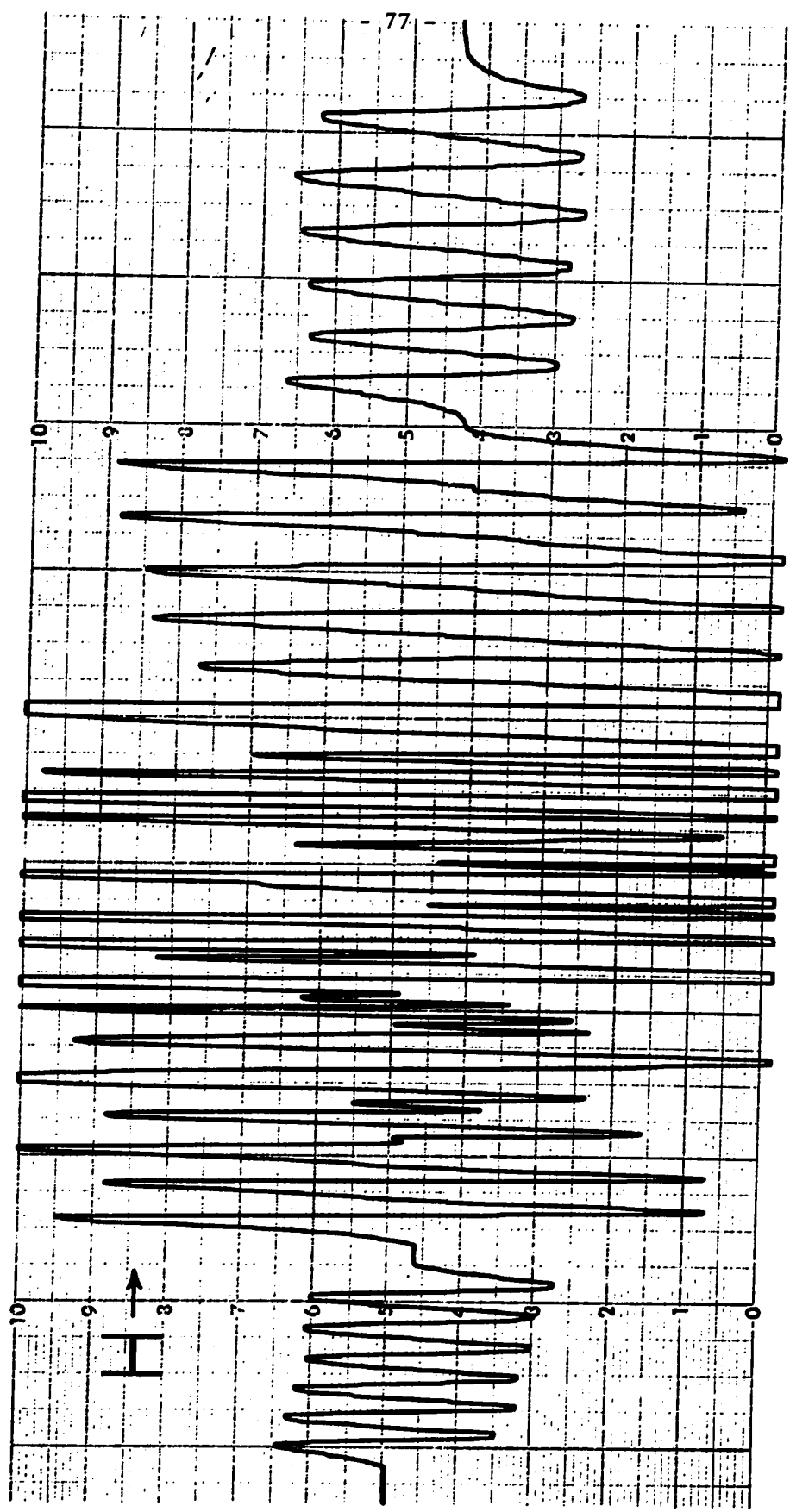


Figure 16. Spectrum of Mn^{2+} in struvite along a magnetic z direction.

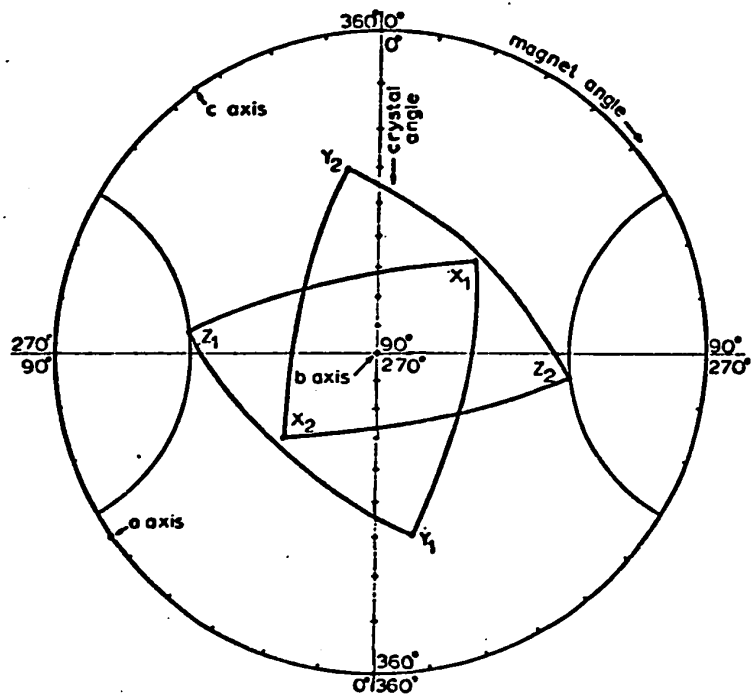


Figure 17. Stereogram showing relationship between the Mn^{2+} magnetic axes and the crystallographic axes for newberyite

Table XI: Angular Relationships between the Magnetic and Crystallographic axes of Mn^{2+} in Newberyite (accuracy $\pm 2\%$)

| Axes | a | b | c | X_2 | Y_2 | Z_2 |
|-------|-------------|------------|-------------|------------|-------------|-------------|
| a | | | | 48° | 110° | 130° |
| b | | | | 43° | 62° | 60° |
| c | | | | 95° | 35° | 125° |
| X_1 | 132° | 43° | 85° | 86° | | |
| Y_1 | 70° | 62° | 145° | | 124° | |
| Z_1 | 50° | 60° | 55° | | | 120° |

Table XII: Magnetic Field Positions of the lowest EPR lines
for each of the Hyperfine Groups of Mn^{2+} in Newberyite
(in gauss) $\nu = 9.27 \text{ GHz}_z$

| | Z axis | Y axis |
|-------|--------|--------|
| H_1 | 1995 | 2028 |
| H_2 | 2490 | 2518 |
| H_3 | 3027 | 3027 |
| H_4 | 3598 | 3590 |
| H_5 | 4187 | 4165 |

Table XIII: Spin Hamiltonian Parameters of Mn^{2+} in Newberyite and Struvite

| | Newberyite | Struvite ³⁹ |
|---------|---|--|
| g | 1.9995 ± 0.0005 | 2.0004 |
| b_2^0 | $253.5 \pm 1.5 \times 10^{-4} \text{ cm}^{-1}$ | $289.0 \times 10^{-4} \text{ cm}^{-1}$ |
| b_2^2 | $252.0 \pm 1.5 \times 10^{-4} \text{ cm}^{-1}$ | $87.6 \times 10^{-4} \text{ cm}^{-1}$ |
| b_4^0 | $-0.79 \pm 0.10 \times 10^{-4} \text{ cm}^{-1}$ | $2.9 \times 10^{-4} \text{ cm}^{-1}$ |
| A | $89.7 \pm 1.5 \times 10^{-4} \text{ cm}^{-1}$ | $88.3 \times 10^{-4} \text{ cm}^{-1}$ |
| B | $88.2 \pm 1.5 \times 10^{-4} \text{ cm}^{-1}$ | $88.5 \times 10^{-4} \text{ cm}^{-1}$ |
| C | - | $87.5 \times 10^{-4} \text{ cm}^{-1}$ |

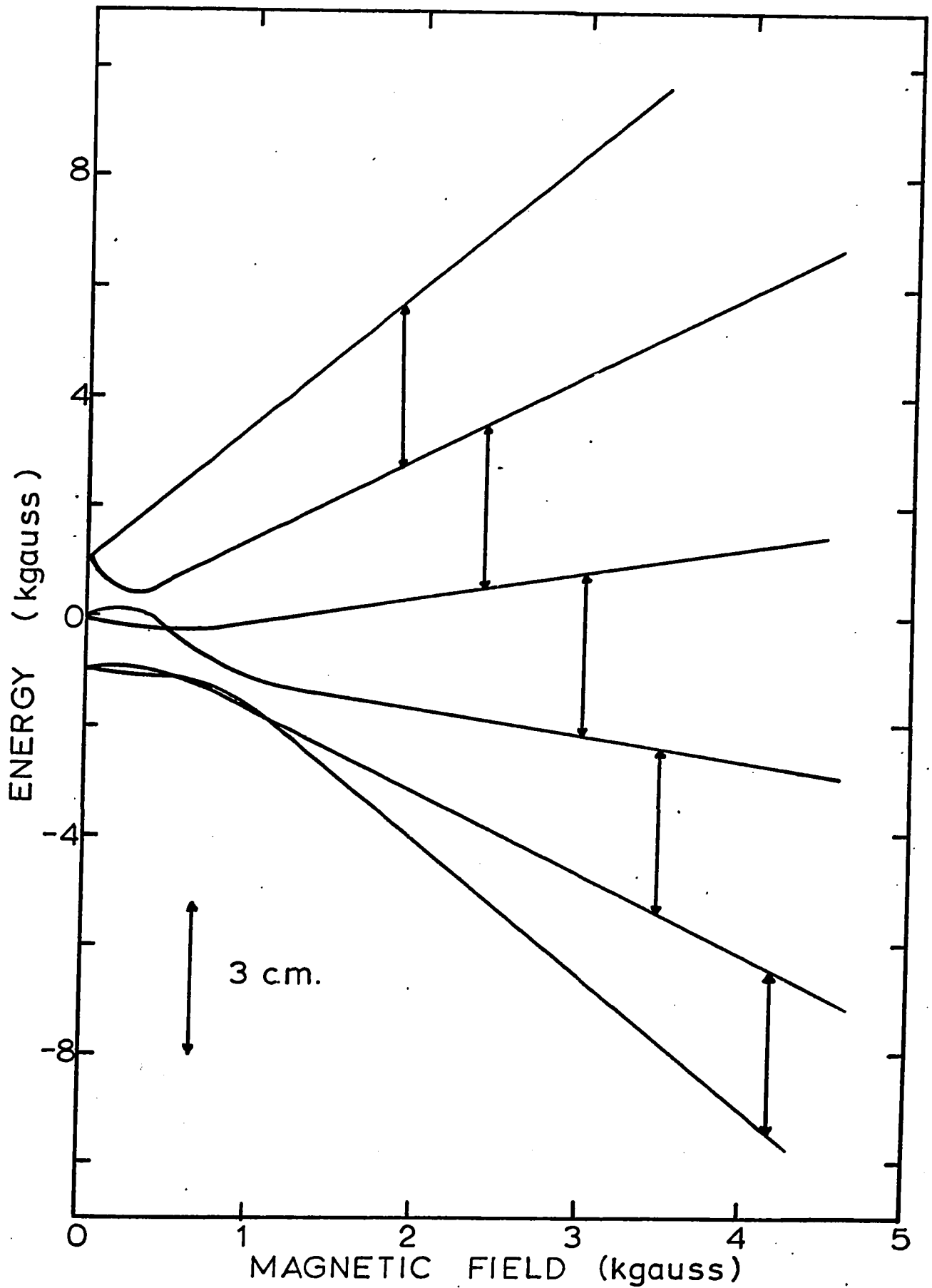


Figure 18. Energy level diagram of Mn²⁺ in newberyite along a magnetic z axis

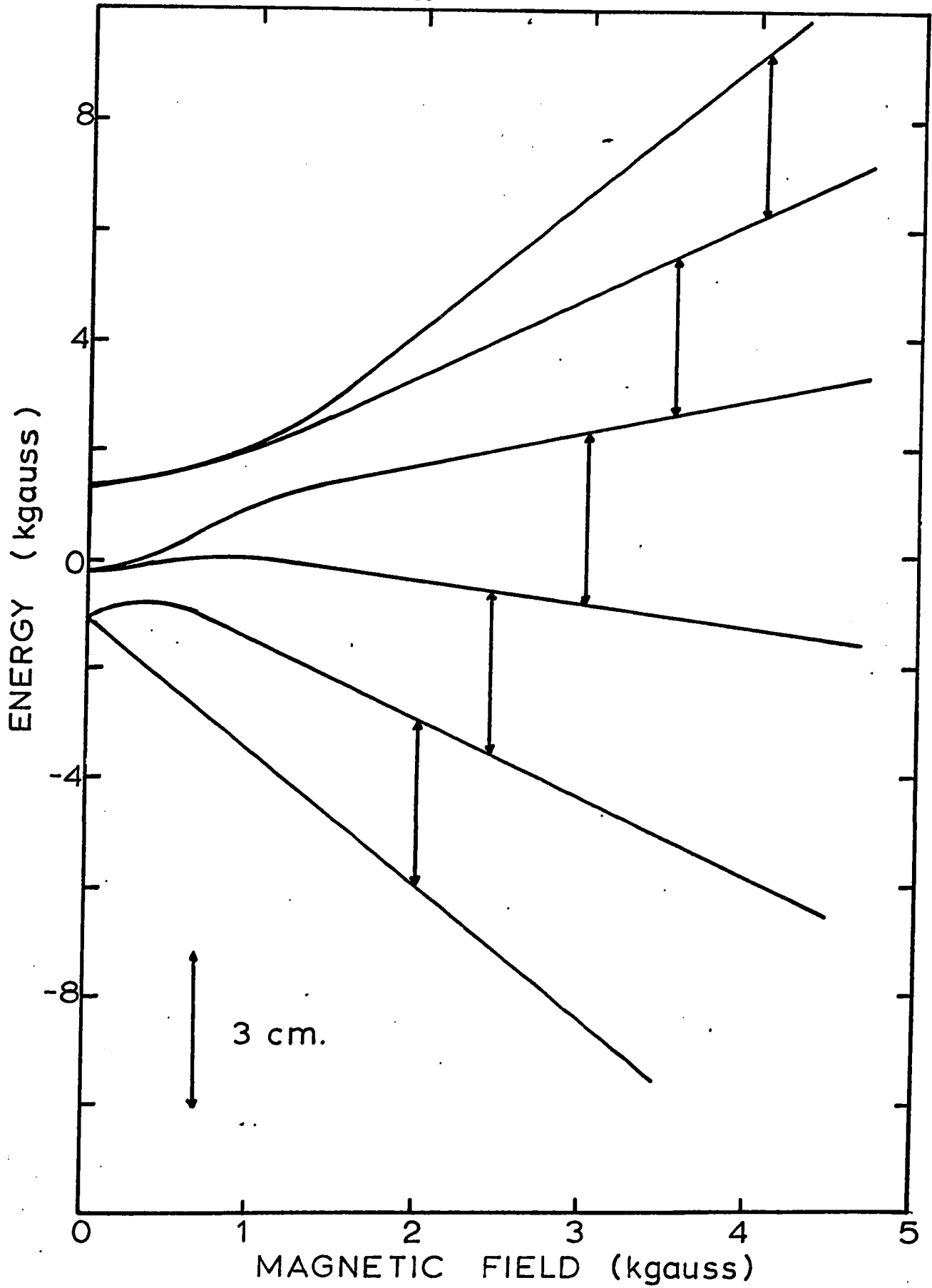


Figure 19. Energy level diagram of Mn²⁺ in newberyite along a magnetic y axis

The results were fitted to a spin Hamiltonian of rhombic symmetry. The spin Hamiltonian parameters were obtained from equations (21), (13), and (14). They are listed in Table XIII along with the parameters for struvite as determined by Vinokurov and Tukhvatullin⁴⁰. Energy level diagrams were drawn for the z and y magnetic axes and are given as Figures 18 and 19. The centers of gravity of the hyperfine groups of lines are also shown in the diagrams.

C. Optical Absorption of Blodite

Using the apparatus shown in Figure 7, the optical absorption spectrum of blodite was obtained. The sample used was about 1/16" thick and it was ground and polished to produce a flat surface. The slice was almost completely transparent except for minor inclusions of unknown origin or composition. The light was focused on an area as free as possible from such inclusions. Upon obtaining the transmitted and incident light recordings, the absorbance was calculated and the spectrum drawn. It is reproduced in Figure 20, but redrawn to an exponential baseline. The peaks of importance for d-d transitions in Mn^{2+} are lettered from a to f. The remaining peaks are unidentified.

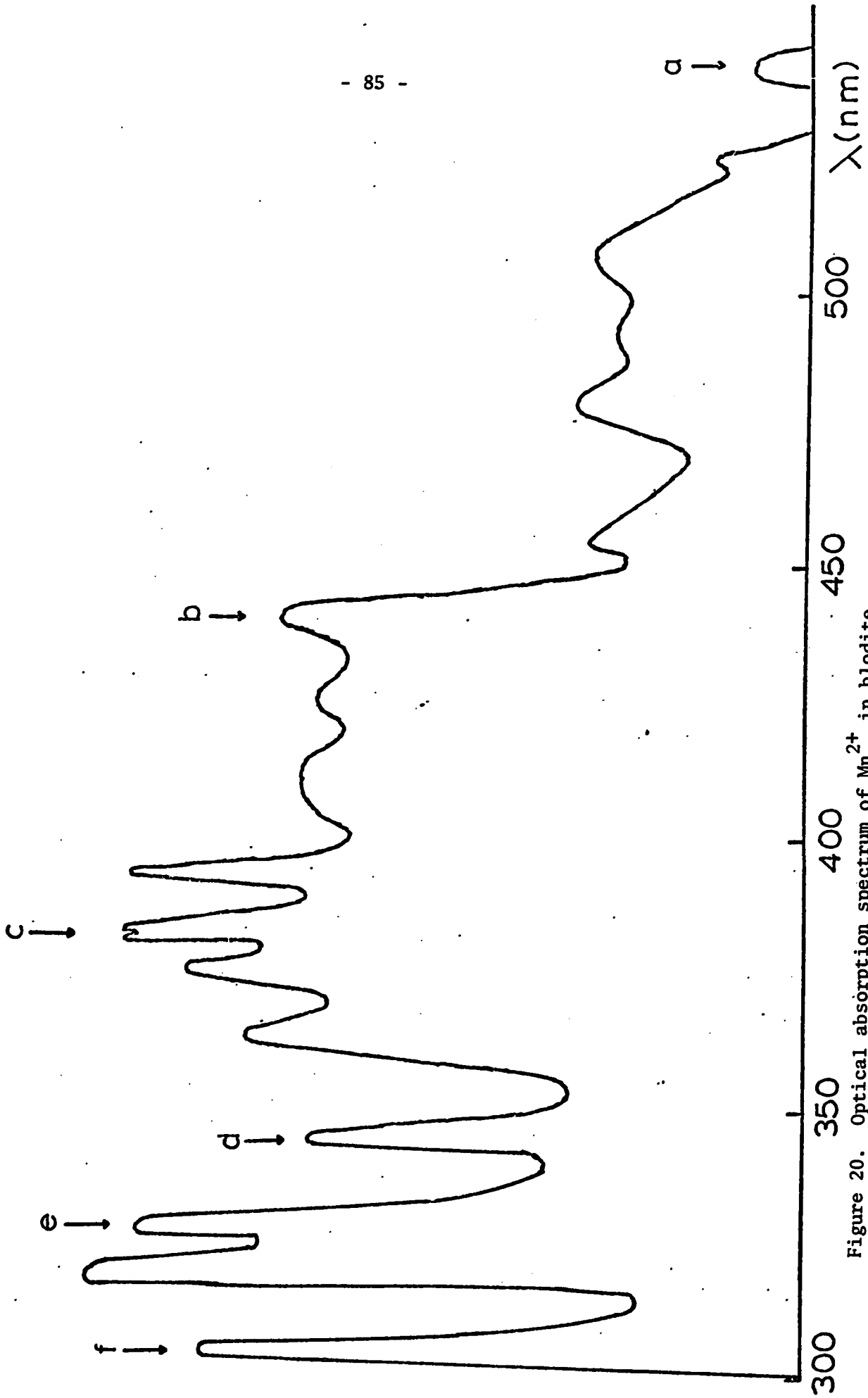


Figure 20. Optical absorption spectrum of Mn²⁺ in blodite

The experiment was repeated and the peaks a to f appeared as before but some of the other peaks did not. Because of the possibility of dirt in the sample, some of these unassigned peaks may be legitimate transitions of the d-d type or possibly of some other type. One reason for the relatively poor quality of the spectrum is that Mn^{2+} is present only as an impurity and, as mentioned previously, line intensities tend to be weak due to various forbidden transition conditions for the $3d^5$ ion. The line positions of the a to f Mn^{2+} peaks are given in Table XIV. The notation used is the same as that discussed in the theory section with the addition that when labelling a crystal field state the parent free ion state is usually placed behind it in brackets.

The choice of the peaks a to f for Mn^{2+} was done with regard to previous Mn^{2+} optical spectra. The transition to ${}^4A_{1g}({}^4E_g({}^4G))$ is a characteristic marking point, as mentioned by several authors. It is often very sharp or split into its two levels by a small amount. Thus this transition was assigned to the peak marked c.

Using the eigenvalues obtained from equation (3) for the two 4E_g levels, and the experimental values of peaks c and e, one

Table XIV: Optical Absorption Peaks of Mn²⁺ in Blodite

| Label | Transitions from the ${}^6A_{1g}({}^6S)$ state to | Value (cm^{-1}) |
|-------|--|-------------------------------|
| a | ${}^4T_{1g}({}^4G)$ | 18,520 |
| b | ${}^4T_{2g}({}^4G)$ | 22,730 |
| c | ${}^4A_{1g} {}^4E_g({}^4G)$ | 26,000 |
| d | ${}^4T_{2g}({}^4D)$ | 28,990 |
| e | ${}^4E_g({}^4D)$ | 30,300 |
| f | ${}^4T_{1g}({}^4P)$ | 32,520 |

obtains values for the Racah parameters as $B = 616 \text{ cm}^{-1}$ and $C = 3,968 \text{ cm}^{-1}$. This is well within the range found by other authors and will be discussed later. Using these values of B and C it is then possible to solve the equations (1) and (2) for the other energy levels as a function of the crystal field splitting parameter $10Dq$. These results are shown in Figure 21. The dotted vertical line indicates the value of $10Dq$ which gives the best fit to the experimentally observed transitions. The comparison between theory and experiment is quite good, except for the ${}^4T_{1g}({}^4P)$ level, as indicated in Table XV.

The value of $10Dq$ is accurate to $\pm 500 \text{ cm}^{-1}$. To include the effects of covalency, the following procedure was used. The values of B and C obtained previously give a C/B ratio of 6.44. Using this ratio as being equal to C_0/B_0 , and the fact that $10B_0 + 5C_0 \sim 27,000 \text{ cm}^{-1}$, computations give $B_0 = 640 \text{ cm}^{-1}$ and $C_0 = 4,120 \text{ cm}^{-1}$. Using these values, and equations (4) and (6), we can compute the eigenvalues corresponding to the ${}^4A_{1g} {}^4E_g ({}^4G)$ level as a function of the covalency parameter ϵ . This is given in Figure 22. If we draw horizontal lines on this graph corresponding to the energy peak c, which is actually a doublet with energies 26,144 and 25,974 cm^{-1} , we obtain a value for ϵ of approximately 0.04. This graph helps confirm the choice of c as the ${}^4A_{1g} {}^4E_g ({}^4G)$ transition. Theory predicts a splitting of about

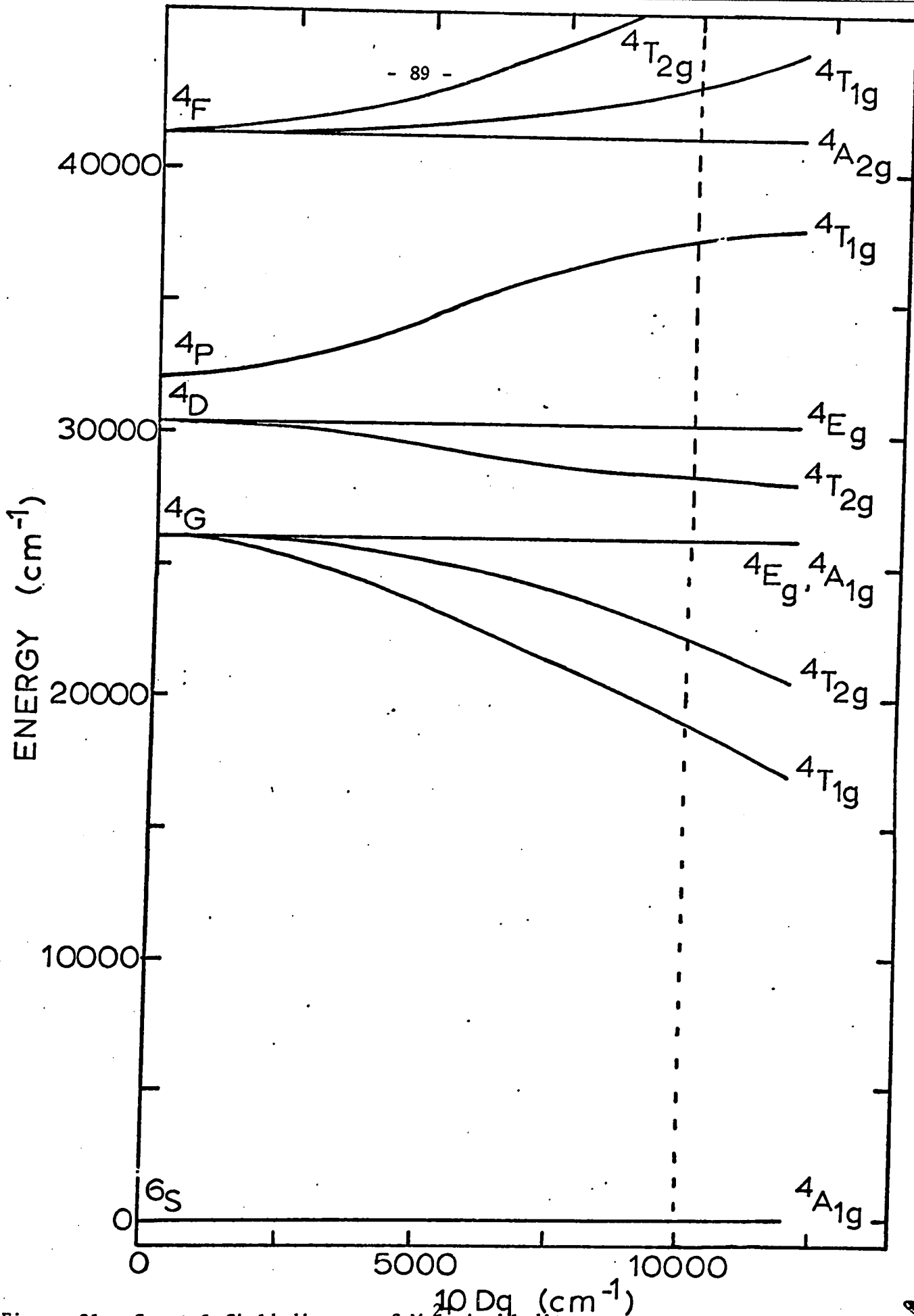


Figure 21. Crystal field diagram of Mn^{2+} in blodite

Table XV: Predicted and Observed Energy Level Values of
 Mn^{2+} in Blodite

| state | predicted (cm^{-1}) (at $Dq = 1000\ cm^{-1}$) | observed (cm^{-1}) |
|------------------------------|---|------------------------|
| ${}^4T_{1g}({}^4G)$ | 18,990 | 18,520 |
| ${}^4T_{2g}({}^4G)$ | 22,360 | 22,730 |
| ${}^4A_{1g}\ {}^4E_g({}^4G)$ | 26,000 | 26,000 |
| ${}^4T_{2g}({}^4D)$ | 28,440 | 28,990 |
| ${}^4E_g({}^4D)$ | 30,310 | 30,300 |
| ${}^4T_{1g}({}^4P)$ | 37,120 | 32,520 |

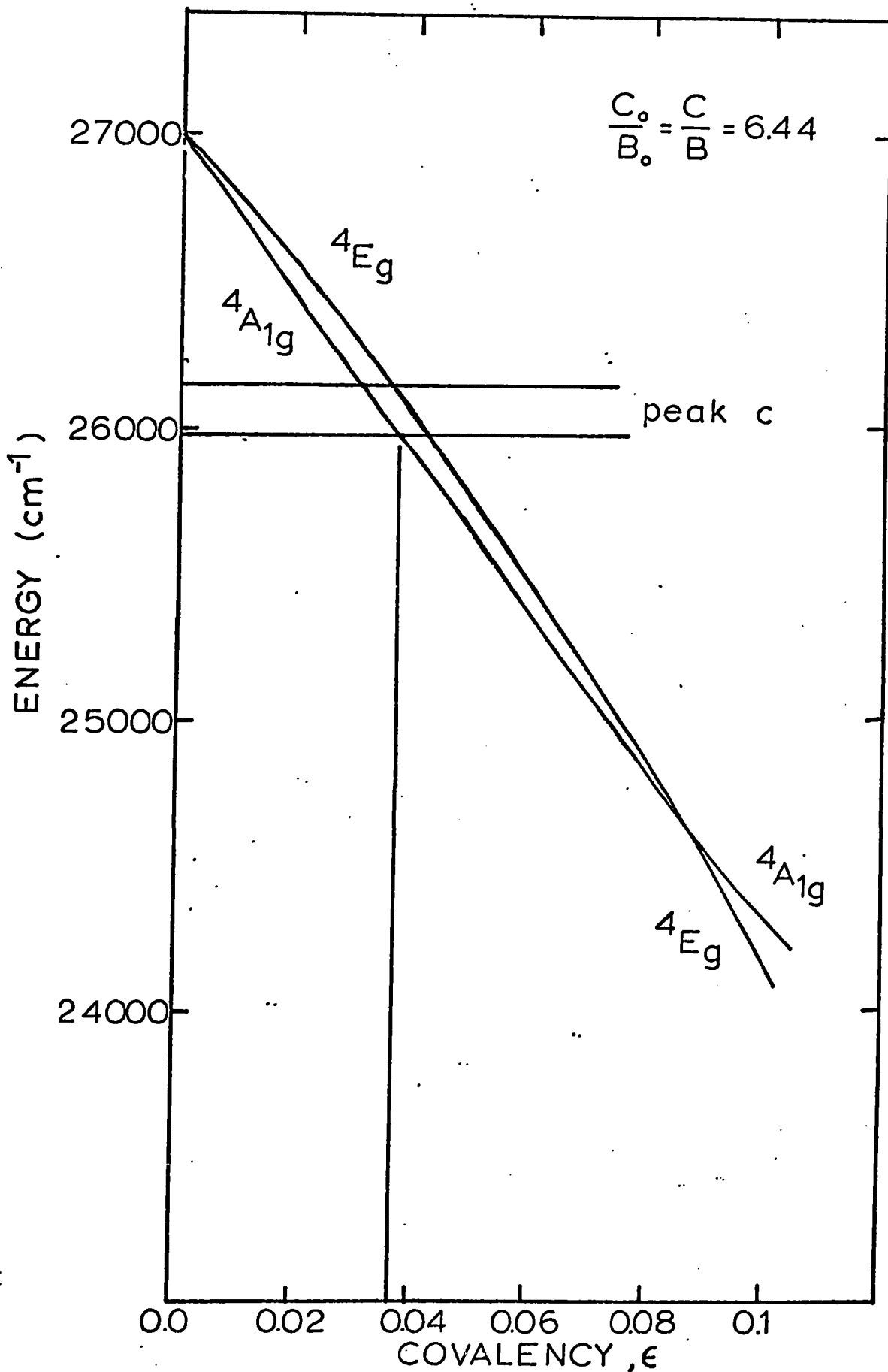


Figure 22. Splitting of $4A_{1g}(4G)$ level as a function of ϵ .

150 cm^{-1} at an energy of $26,000 \text{ cm}^{-1}$ for $\epsilon = 0.039$. Experimentally, we find the splitting to equal 170 cm^{-1} . Now, having obtained values for B_0 , C_0 and ϵ , we can solve equations (4) through (8) as a function of $10Dq'$ and we obtain the results plotted in Figure 23. The best fit to experiment now occurs at $10Dq' = 11,000 \text{ cm}^{-1}$. The comparison between experimental and calculated line positions is shown in Table XVI.

The fit is quite good except again for the ${}^4T_{1g}({}^4P)$ level. Several authors have also noted this discrepancy in their studies of Mn^{2+} .

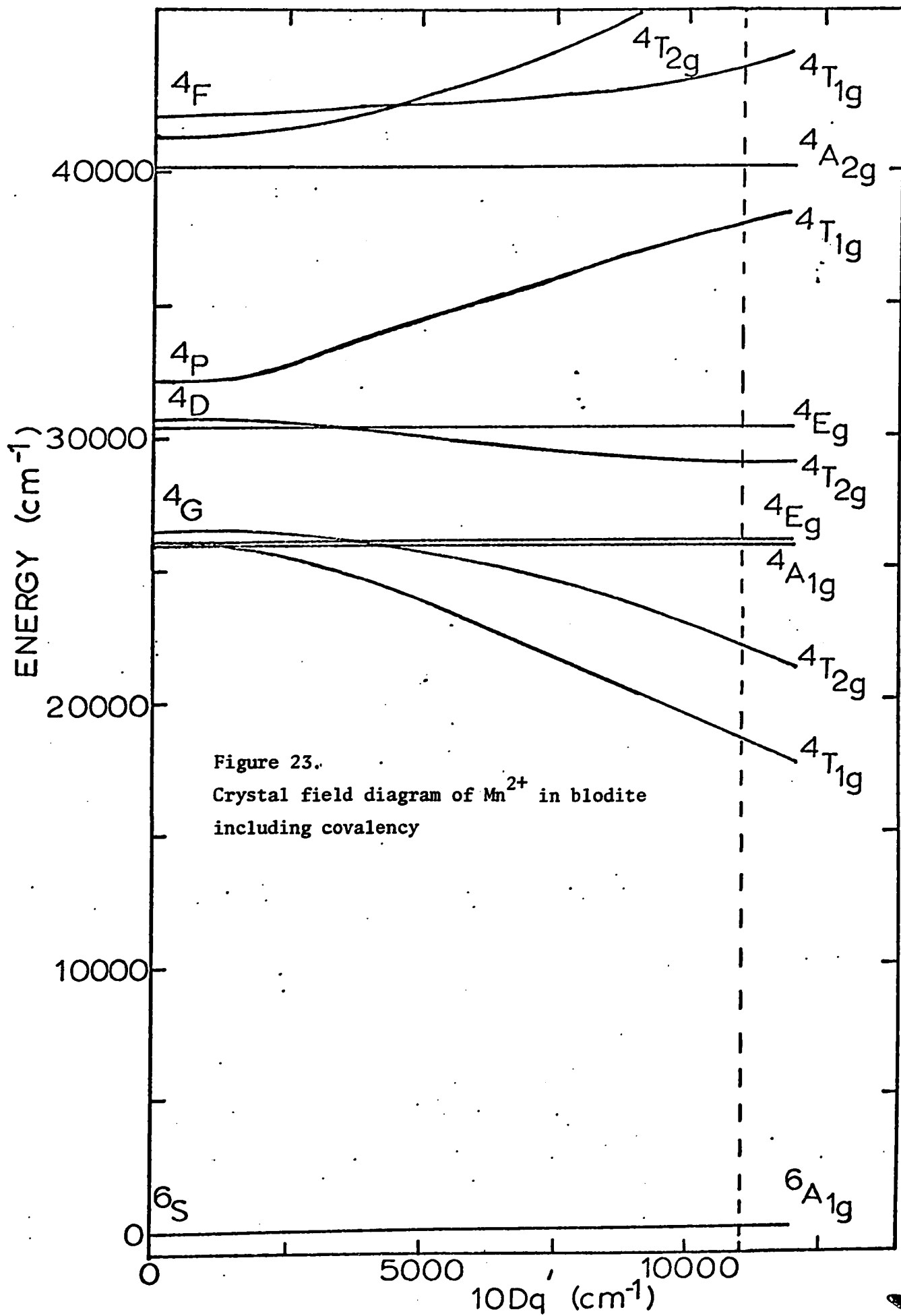


Figure 23.
Crystal field diagram of Mn²⁺ in blodite
including covalency

Table XVI: Comparison of Calculated and Observed Line Positions
in the Optical Spectrum of Mn^{2+} in Blodite at
 $10Dq' = 11,000 \text{ cm}^{-1}$ and $\epsilon = 0.04$

| | observed (cm^{-1}) | calculated (cm^{-1}) |
|---------------------|-------------------------------|---------------------------------|
| ${}^4T_{1g}({}^4G)$ | 18,520 | 18,570 |
| ${}^4T_{2g}({}^4G)$ | 22,730 | 22,050 |
| ${}^4A_{1g}({}^4G)$ | 25,970 | 25,930 |
| ${}^4E_g({}^4G)$ | 26,140 | 26,020 |
| ${}^4T_{1g}({}^4D)$ | 28,990 | 29,000 |
| ${}^4E_g({}^4D)$ | 30,300 | 30,330 |
| ${}^4T_{1g}({}^4P)$ | 32,520 | 37,910 |

Chapter VI

Conclusions

A. EPR of Blodite and Newberyite

In both blodite and newberyite, the EPR results are in accord with other Mn^{2+} EPR studies done to date. The g-values exhibit a negative departure from the free spin value as predicted by Watanabe³¹ and found for several other manganese compounds as listed in Table XVII.

Some of the compounds in Table XVII do not have isotropic g-values and in those cases an average g-value has been listed.

The parameters b_2^0 and b_2^2 are a measure of the axial and rhombic distortion of the paramagnetic ion site, and the calculations for both blodite and newberyite indicate a strong rhombic distortion. In newberyite the rhombic parameter b_2^2 is approximately equal to the axial parameter b_2^0 . In struvite, the rhombic distortion is reported as being smaller than b_2^0 .

Table XVII: Some G-Values for Mn^{2+} in various Compounds

| Compound | G-value (s) | Reference |
|---|-------------|-------------------------------------|
| Blodite ($Na_2Mg(SO_4)_2 \cdot 4H_2O$) | 1.9993 | this work |
| Newberyite ($MgHPO_4 \cdot 3H_2O$) | 1.9995 | this work |
| Struvite ($MgNH_4PO_4 \cdot 6H_2O$) | 2.0004 | Vinokurov et.al. ³⁹ |
| Manganese Fluosilicate ($MnSiF_6 \cdot 6H_2O$) | 2.0000 | Bleaney and Abragam ⁴¹ |
| Tutton Salt ($Mn(NH_4)_2(SO_4)_2 \cdot 6H_2O$) | 1.9980 | Bleaney and Abragam ⁴¹ |
| MgO | 2.0015 | Low ⁴² |
| CaF ₂ | 2.0013 | Low ⁴² |
| Morinite ($Ca_4Na_2Al_4(F,OH)_{10}(PO_4)_4 \cdot 3H_2O$) | 2.0015 | Manoogian and Hsu ⁴³ |
| Monticellite ($MgCaSiO_4$) | 1.9930 | Danilov and Manoogian ⁴² |

Table XVII: Some G-Values for Mn^{2+} in various Compounds

| | | |
|---|--------|--------------------------------|
| Diopside ($CaMgSi_2O_6$) | 2.0016 | Vinokurov et.al. ²⁷ |
| Tremolite ($H_2Ca_2Mg_5(SiO_3)_8$) | 1.9960 | Manoogian ⁴⁵ |
| $CaSO_4$ | 1.9960 | Takeda ⁴⁶ |
| Brucite ($Mg(OH)_2$) | 2.0003 | Pieczonka et.al. ⁴⁷ |
| $Zn(ClO_4)_2 \cdot 6H_2O$ | 1.9990 | Fritz and Yarmus ⁴⁸ |

It is not possible to tell which of the two Mn^{2+} magnetic complexes belongs to the two inequivalent magnesium sites in the crystals. In Figure 1, the two possible z axis directions are indicated for blodite.

The magnitudes of the hyperfine splitting constants A and B are a measure of the amount of covalent bonding between the paramagnetic ion and the surrounding ligands, as established by Van Wieringen⁴, Henning⁶, Maturuma⁵, and Simanek and Muller⁷. The results indicate that an increase in the hyperfine splitting corresponds to a decrease in covalency. The covalency of a complex is defined by Pauling's⁸ covalency parameter c, and when this is divided by the number of ligands n, we get the average covalency per bond. Several plots of the hyperfine splitting versus the quantity c/n have been produced^{5,6,7}. For the purposes of this paper we will use the monotonic part of Simanek and Muller's⁷ plot, which is reproduced as Figure 24. Table XVIII gives a list of hyperfine parameters for Mn^{2+} in various environments. An average is made of the values of A and B whenever available, because the graph in Figure 24 is itself plotted through average values of A for a particular series of crystals. The idea is to use Figure 24 to account for the variation in hyperfine parameters for Mn^{2+} in complicated systems

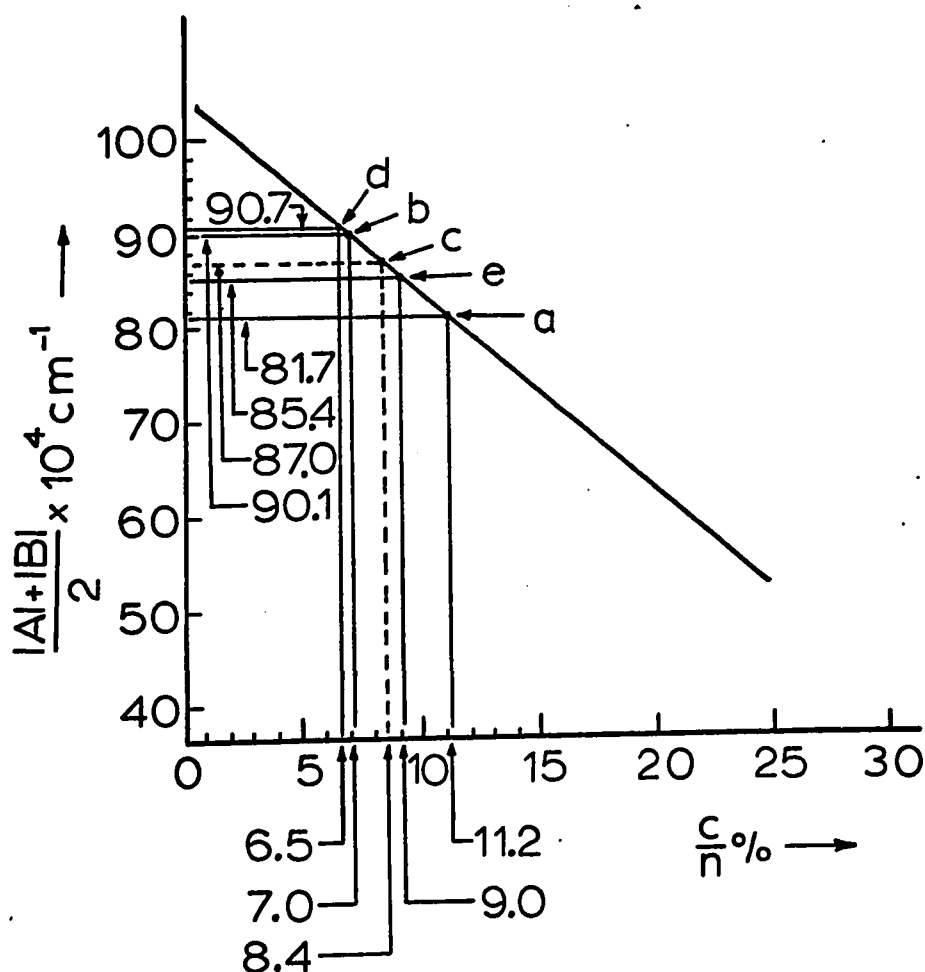


Figure 24. Monatomic plot of the hyperfine interaction constant A of Mn^{2+} versus the covalency parameter c divided into the number of ligand n (taken from Simanek and Muller⁷)

- a - coordination of 6O^{2-}
- b - coordination of $6\text{H}_2\text{O}$
- c - coordination of $4\text{H}_2\text{O} \cdot 2\text{O}^{2-}$
- d - coordination of 6F^-
- e - coordination of $3\text{H}_2\text{O} \cdot 3\text{O}^{2-}$

Table XVIII: Comparison of hyperfine parameters for Mn^{2+} in some Crystals (in units of $10^4 cm^{-1}$).

| Crystal | Coordinated Ligands | A | B | $\frac{ A + B }{2}$ | References |
|---|--------------------------|--------------------|--------------|-----------------------|----------------------------------|
| Blodite | $4H_2O, 2O^{2-}$ | 89.0 | 86.4 | 87.7 | this work |
| Newberyite | $3H_2O, 3O^{2-}$ | 89.7 | 88.2 | 89.0 | this work |
| Struvite | $6H_2O$ | 88.3 (c = 87.5) | 88.5 | 88.1 | Ref. 40 |
| Morinite | $3H_2O? 3F^-?$ | 91.8 | 93.2 | 92.5 | Ref. 43 |
| Tutton Salt | $6H_2O$ | 91.9 | - | 91.1 | Ref. 41 |
| Fluosilicate | $6H_2O$ | 96.1 | 93.3 | 94.7 | Ref. 41 |
| Perchlorate | $6H_2O$ | 89.5 | 89.8 | 89.6 | Ref. 48 |
| Monticellite | $6O^{2-}$ | 79.9 | 79.9 | 79.9 | Ref. 44 |
| Diopside (2 sites) | $6O^{2-}$ & $8O^{2-}$ | 78.9 85.4 | 78.9 85.7 | 78.9 85.5 | Ref. 27 |
| MgO | $6O^{2-}$ | 81.0 | - | 81.0 | Ref. 42 |
| CaF_2 | $8F^-$ | 95.5 | - | 95.5 | Ref. 42 |
| Brucite | $6OH^-$ | 85.7 | 84.9 | 85.4 | Ref. 47 |
| Apatite ($Ca_5(PO_4)_3(F,Cl,OH)$) | $9O^{2-}$ | 86.4 | 88.1 | 87.2 | Vinokurov et.al. ⁴⁹ |
| Forsterite (Mg_2SiO_4) | $6O^{2-}$ | 84.1 | - | 84.1 | Chaletaine & Weeks ⁵⁰ |
| GASH ($C(NH_2)_3Al(SO_4)_2 \cdot 6H_2O$) | $6H_2O$ | 87.5 | - | 87.5 | Milsch & Windsch ⁵¹ |

with coordinated ligands of mixed types such as in blodite and newberyite.

For a coordination of $6O^{2-}$ about Mn^{2+} , we see a variation of the hyperfine parameter in Figure 24 with the type of crystal. To obtain a value of $(|A| + |B|)/2$ for a typical $Mn^{2+} - 6O^{2-}$ complex, we averaged the values for monticellite, forsterite and MgO. This gives a value of $81.7 \times 10^{-4} \text{ cm}^{-1}$, which, from Figure 24, corresponds to a covalency value of $c/n = 11.2\%$. In a similar manner, an average of the $(|A| + |B|)/2$ values for tutton salt, fluosilicate, struvite, GASH, and perchlorate gives a value of $90.1 \times 10^{-4} \text{ cm}^{-1}$ for the $Mn^{2+} - 6H_2O$ complex. From Figure 24, this gives a covalency of $c/n = 7.0\%$.

In the case of blodite, the manganese ion is coordinated by four water molecules and two oxygens, and an average covalency may be computed as $(4 \times 7.0 + 2 \times 11.2)/6 = 8.4\%$. From Figure 24, this corresponds to an average hyperfine parameter of $87.0 \times 10^{-4} \text{ cm}^{-1}$, which is close to the $(|A| + |B|)/2$ value found experimentally for Mn^{2+} in blodite, which is $87.7 \times 10^{-4} \text{ cm}^{-1}$. In newberyite, the coordinated ligands are three waters and three oxygens, and the computation gives

an average covalency of $(3 \times 11.2 + 3 \times 7.0)/6 = 9.1\%$, thus corresponding to a $(|A| + |B|)/2$ value of $86.0 \times 10^{-4} \text{ cm}^{-1}$. The experimental value of $(|A| + |B|)/2$ in newberyite is $89.0 \pm 1.5 \times 10^{-4} \text{ cm}^{-1}$. The agreement here is not as good as in the case of blodite which could indicate a more complicated bonding involving other atoms in the unit cell. In any case, the agreement is good enough in both minerals to verify the relationship between the magnitude of the hyperfine splitting for various coordinated ligands and the covalency.

B. Optical Absorption of Blodite

The line positions of the optical transitions for blodite can be compared favourably with other optical studies of Mn^{2+} in various compounds. This comparison is summarized in Table XIX. It appears that the energy of the ${}^4A_{1g} {}^4E_g ({}^4G)$ level found for blodite is slightly greater than that reported for some other crystals. This might indicate the peak before c on Figure 20 is the correct level. This was discounted by us because of the good fit obtained theoretically, with the ${}^4A_{1g} {}^4E_g ({}^4G)$ level being fundamental to this fit. Also, the doublet structure has the proper separation as predicted by Figure 22.

Table XIX: Comparison of Optical Absorption Line Positions for Mn^{2+} in Various Compounds (in cm^{-1}).

| Transitions from | Blodite | Pyroxmangite ⁵³ | Lepidolite ⁵⁴ | ZnSe ⁵⁵ | KMnF ₃ ⁵⁶ | RbMnF ₃ ⁵⁶ | KClMn ² ⁵⁷ | MnO ¹⁷ | MnF ₂ ²³ | Perchlorate ² |
|------------------------|---------|----------------------------|--------------------------|--------------------|---------------------------------|----------------------------------|----------------------------------|-------------------|--------------------------------|--------------------------|
| ${}^6A_{1g}({}^6S)$ to | | | | | | | | | | |
| ${}^4T_{1g}({}^4G)$ | 18520 | 18200 | 18500 | 18870 | | | 19300 | 16393 | 19440 | 18870 |
| ${}^4T_{2g}({}^4G)$ | 22730 | 23000 | 23200 | 20018 | | | 22700 | 20833 | 23500 | 23120 |
| ${}^4A_{1g}({}^4G)$ | 25970 | 23950 | 24000 | 21410 | 25190 | 25200 | 23880 | 23810 | 25250 | 24960 |
| ${}^4E_g({}^4G)$ | 26140 | 24400 | 24200 | 21410 | 25500 | 25400 | 23880 | 23810 | 25500 | 25275 |
| ${}^4T_{2g}({}^4D)$ | 28990 | | | | 28070 | 28110 | 27200 | | 28200 | 27980 |
| ${}^4E_g({}^4D)$ | 30300 | | | | 30030 | 30070 | 28135 | | 30230 | 20750 |
| ${}^4T_{1g}({}^4P)$ | 32520 | | | | 32630 | 32630 | | | 33060 | 32960 |

Because of the high value for this level, the ratio of the Racah parameters is also high, the value being $C/B = 6.44$. Most authors quote a value of about 4 to 5 for this ratio. Table XX compares crystal field parameters for blodite and several other minerals. There appears to be no consistent pattern between the nature of the ligands and the ratio C/B . Orgel⁵² pointed out that $10D_q$ should increase in the coordination sequence of Cl^- to F^- to H_2O , and this is verified in Table XX.

The value of the covalency parameter for blodite, $\epsilon = 0.04$, is lower than the covalency predicted by the EPR hyperfine splitting of 0.084. The reason for this discrepancy may be in the site symmetry. The spin Hamiltonian parameters b_2^0 and b_2^2 obtained for blodite indicate distortions from cubic symmetry in the crystal field. The crystal field matrices used in the optical studies involve only cubic symmetry. For example, Koide and Pryce² have shown that a rhombic distortion will depress one of the 4E_g levels of the ${}^4A_{1g} {}^4E_g ({}^4G)$ group. The crystal field matrices are also approximate in that they only include first order effects of an electrostatic nature and the covalency, neglecting the complications of spin-orbit, spin-spin, and vibronic interactions. In Stout's²³ work of MnF_2 , his covalency works out to 0.0645. From Simanek and Muller's⁷ plot

Table XX: Comparison of Crystal Field Parameters in Various Crystals
(in cm^{-1})

| Crystal | B | C | 10DQ | B_0 | C_0 | 10Dq' | ϵ | $C/B = C_0/B_0$ |
|--|-----|------|-------|-------|-------|-------|------------|-----------------|
| Blodite | 616 | 3968 | 10000 | 640 | 4120 | 11000 | 0.04 | 6.44 |
| MnF_2 ²³ | - | - | - | 950 | 3280 | 7800 | 0.0645 | 3.45 |
| Mn^{2+} in water ²⁰ | 671 | 3710 | 8480 | 786 | 379- | - | - | 5.53 |
| Mn^{2+} in water ²² | - | - | - | 860 | 3850 | 12300 | - | 4.48 |
| Mn^{2+} in water ⁵² | - | - | 7900 | - | - | - | - | - |
| Mn^{2+} in water ⁵⁸ | - | - | 7800 | - | - | - | - | - |
| MnO ¹⁷ | 786 | 3210 | 9790 | - | - | - | - | 4.08 |
| KCl:Mn^{2+} ⁵⁷ | 760 | 2955 | 5900 | - | - | - | - | 3.89 |
| ZnSe ⁵⁵ | 660 | 2970 | 5000 | - | - | - | - | 4.50 |
| KMnF_3 ⁵⁶ | - | - | 7311 | 917 | 3271 | - | 0.0649 | 3.57 |
| RbMnF_3 ⁵⁶ | - | - | 7304 | 917 | 3271 | - | 0.0645 | 3.57 |
| CsMnF_3 ⁵⁶ | - | - | 7865 | 917 | 3271 | - | 0.0653 | 3.57 |

of hyperfine splitting versus Pauling's covalency, we get a value of 0.0633 for the covalency of MgF_2 . The good agreement is as expected since the MgF_2 paramagnetic ion site is much less distorted than the blodite site⁵⁹.

In summary, the EPR of Mn^{2+} in blodite and newberyite has been investigated and the results compared with other reported EPR work on Mn^{2+} . A simple method is given to determine the covalency of a complex consisting of mixed types of ligands. The optical absorption of Mn^{2+} in blodite was investigated and the resulting crystal field parameters were compared with other optical studies of Mn^{2+} . The covalency of the Mn^{2+} site in blodite was also determined from optical studies and the results compared with the value obtained by EPR studies.

Appendix

The Matrix Elements of the Spin Hamiltonian with $S = 5/2$ and $I = 5/2$.

The matrix elements are defined by $\langle M_S, M_I | M_S, M_I \rangle$ where

$$M_S = +S, +S - 1, \dots, -S$$

and

$$M_I = +I, +I - 1, \dots, -I$$

Since the matrix is symmetric, only the upper triangle is considered; the lower triangle can be obtained from this information. Any elements of the upper triangle not listed are zero. The parameters are as defined previously.

Also included is the FORTRAN IV computer program for the diagonalization of the 36×36 matrix of the ground state, the program for obtaining the crystal field states, and the program used to theoretically calculate the ground state zero field splitting. The diagonalization program, EIGEN, is an IBM-supplied standard library sub-program.

Diagonal Elements of Hamiltonian Matrix

$$\begin{aligned} \langle 5/2, \pm 5/2 | 5/2, \pm 5/2 \rangle &= X_1 \pm 25/4 A \\ \langle 5/2, \pm 3/2 | 5/2, \pm 3/2 \rangle &= X_1 \pm 15/4 A \\ \langle 5/2, \pm 1/2 | 5/2, \pm 1/2 \rangle &= X_1 \pm 5/4 A \\ \langle 3/2, \pm 5/2 | 3/2, \pm 5/2 \rangle &= X_2 \pm 15/4 A \\ \langle 3/2, \pm 3/2 | 3/2, \pm 3/2 \rangle &= X_2 \pm 9/4 A \\ \langle 1/2, \pm 5/2 | 1/2, \pm 5/2 \rangle &= X_3 \pm 5/4 A \\ \langle 1/2, \pm 3/2 | 1/2, \pm 3/2 \rangle &= X_3 \pm 3/4 A \\ \langle 1/2, \pm 1/2 | 1/2, \pm 1/2 \rangle &= X_3 \pm 1/4 A \\ \langle -1/2, \pm 5/2 | -1/2, \pm 5/2 \rangle &= X_4 \mp 5/4 A \\ \langle -1/2, \pm 3/2 | -1/2, \pm 3/2 \rangle &= X_4 \mp 3/4 A \\ \langle -1/2, \pm 1/2 | -1/2, \pm 1/2 \rangle &= X_4 \mp 1/4 A \\ \langle -3/2, \pm 5/2 | -3/2, \pm 5/2 \rangle &= X_5 \mp 15/4 A \\ \langle -3/2, \pm 3/2 | -3/2, \pm 3/2 \rangle &= X_5 \mp 3/4 A \\ \langle -3/2, \pm 1/2 | -3/2, \pm 1/2 \rangle &= X_5 \mp 3/4 A \\ \langle -5/2, \pm 5/2 | -5/2, \pm 5/2 \rangle &= X_6 \mp 25/4 A \\ \langle -5/2, \pm 3/2 | -5/2, \pm 3/2 \rangle &= X_6 \mp 15/4 A \\ \langle -5/2, \pm 1/2 | -5/2, \pm 1/2 \rangle &= X_6 \mp 9/4 A \end{aligned}$$

where

$$X_1 = 5/2 g_z \beta H_z + 10/3 b_2^0 + b_4^0$$

$$X_2 = 3/2 g_z \beta H_z - 2/3 b_2^0 - 3b_4^0$$

$$X_3 = 1/2 g_z \beta H_z - 8/2 b_2^0 + 2b_4^0$$

$$X_4 = -1/2 g_z \beta H_z - 8/2 b_2^0 + 2b_4^0$$

$$X_5 = -3/2 g_z \beta H_z - 2/2 b_2^0 - 3b_4^0$$

$$X_6 = -5/2 g_z \beta H_z + 10/3 b_2^0 + b_4^0$$

Off-Diagonal Elements

$$\langle 5/2, \pm 5/2 \mid 3/2, \pm 3/2 \rangle = \langle 5/2, \mp 3/2 \mid 3/2, \mp 5/2 \rangle = 5/4 (B \mp C)$$

$$\langle 5/2, \pm 3/2 \mid 3/2, \pm 1/2 \rangle = \langle 5/2, \mp 1/2 \mid 3/2, \mp 3/2 \rangle = \sqrt{10}/2 (B \mp C)$$

$$\langle 5/2, \pm 1/2 \mid 5/2 \mp 1/2 \rangle = 3\sqrt{5}/4 (B \mp C)$$

$$\langle 5/2, M_I \mid 1/2, M_I' \rangle = \sqrt{10/3} b_2^2 + 3\sqrt{10}/20 b_4^2 \quad \text{for } M_I = M_I'$$

$$\langle 5/2, M_I \mid 3/2, M_I' \rangle = \sqrt{5/5} b_4^4 \quad \text{for } M_I = M_I'$$

$$\langle 3/2, \pm 5/2 \mid 1/2, \pm 3/2 \rangle = \langle 3/2, \mp 3/2 \mid 1/2, \mp 5/2 \rangle = \sqrt{10}/2 (C \mp B)$$

$$\langle 3/2, \pm 3/2 \mid 1/2, \pm 1/2 \rangle = \langle 3/2, \mp 1/2 \mid 1/2, \mp 3/2 \rangle = 2(C \mp B)$$

$$\langle 3/2, \pm 1/2 \mid 1/2, 1/2 \rangle = 3\sqrt{2}/2 \quad (C \mp B)$$

$$\langle 3/2, M_I \mid -1/2, M_I' \rangle = \sqrt{2} b_2^2 - \sqrt{2}/4 b_4^2 \quad \text{for } M_I = M_I'$$

$$\langle 3/2, M_I \mid -5/2, M_I' \rangle = \sqrt{5}/5 b_4^4 \quad \text{for } M_I = M_I'$$

$$\langle 1/2, \pm 5/2 \mid -1/2, \pm 3/2 \rangle = \langle 1/2, \mp 3/2 \mid -1/2, \mp 5/2 \rangle = 3\sqrt{5}/4 \quad (C \mp B)$$

$$\langle 1/2, \pm 3/2 \mid -1/2, \pm 1/2 \rangle = \langle 1/2, \mp 1/2 \mid -1/2, \mp 3/2 \rangle = 3\sqrt{2}/2 \quad (C \mp B)$$

$$\langle 1/2, \pm 1/2 \mid -1/2, \mp 1/2 \rangle = 9/4 \quad (C \mp B)$$

$$\langle 1/2, M_I \mid -3/2, M_I' \rangle = \sqrt{2}/2 b_2^2 - \sqrt{2}/4 b_4^2 \quad \text{for } M_I = M_I'$$

$$\langle -1/2, \pm 5/2 \mid -3/2, \pm 3/2 \rangle = \langle -1/2, \mp 3/2 \mid -3/2, \mp 5/2 \rangle = \sqrt{10}/2 \quad (C \mp B)$$

$$\langle -1/2, \pm 3/2 \mid -3/2, \mp 1/2 \rangle = \langle -1/2, \mp 1/2 \mid -3/2, \mp 3/2 \rangle = 2(C \mp B)$$

$$\langle -1/2, \pm 1/2 \mid -3/2, \mp 1/2 \rangle = 3\sqrt{2}/2 \quad (C \mp B)$$

$$\langle -1/2, M_I \mid -5/2, M_I' \rangle = \langle 5/2, M_I \mid 1/2, M_I' \rangle \quad \text{for } M_I = M_I'$$

$$\langle -3/2, \pm 5/2 \mid -5/2, \pm 3/2 \rangle = \langle -3/2, \mp 3/2 \mid -5/2, \mp 5/2 \rangle = 5/4 \quad (B \mp C)$$

$$\langle -3/2, \pm 3/2 \mid -5/2, \pm 1/2 \rangle = \langle -3/2, \mp 1/2 \mid -5/2, \mp 3/2 \rangle = \mp\sqrt{10}/2 \quad (B \mp C)$$

$$\langle -3/2, \pm 1/2 \mid -5/2, \mp 1/2 \rangle = \mp 3\sqrt{5}/4 \quad (B \mp C)$$


```

0024 AHF=BHF
0025 BHF=AHF
0026 WRITE(2,3001)
0027 FORMAT(4X,'MAGNET IN X DIRECTION',/)
0028 GO TO 1000
0029 3000 B02=-0.5*(B02+B22)
0030 B22=0.5*(3.0*B02-B22)
0031 B04=C.125*(3.0*B04+B24+B44)
0032 B24=-0.5*(5.0*B04+B24-B44)
0033 B44=C.125*(35.0*B04-7.0*B24+B44)
0034 AHF=CHF
0035 BHF=AHF
0036 CHF=RHF
0037 WRITE(3,2001)
0038 2001 FORMAT(40X,'MAGNET IN Y DIRECTION',/)
0039 1000 H=2.0E+04
0040 13 CONTINUE
0041 DO 14 I=1,566
0042 14 A(I)=0.0
0043 GO TO 11
0044 783 FA=2.5*H+((1.0*C*B02)/3.0)+B04
0045 789 A(1)=FA+(25.0*AHF)/4.0
0046 A(3)=FA+(15.0*AHF)/4.0
0047 A(6)=FA+(5.0*AHF)/4.0
0048 A(10)=FA-(5.0*AHF)/4.0
0049 A(15)=FA-(15.0*AHF)/4.0
0050 A(21)=FA-(25.0*AHF)/4.0
0051 A(23)=1.25*(BHF+CHF)
0052 FB=1.5*H-((2.0*C*B02)/3.0)-3.0*B04
0053 A(28)=FB+(15.0*AHF)/4.0
0054 A(29)=1.25*(CHF-RHF)
0055 A(31)=(SORT(10.)*(CHF+BHF))/2.0
0056 A(36)=FB+(9.0*AHF)/4.0
0057 A(38)=(SORT(10.)*(CHF-RHF))/2.0
0058 A(40)=(3.0*SQR*(5.)*(CHF+BHF))/4.0
0059 A(45)=FB+0.75*AHF
0060 A(48)=(3.0*SORT(5.)*(CHF-BHF))/4.0
0061 A(50)=A(31)
0062 A(55)=FB-0.75*AHF
0063 A(59)=A(28)
0064 A(61)=A(23)
0065 A(66)=FB-(9.0*AHF)/4.0
0066 A(71)=A(29)

```

```

0067 A(78)=F3-3.75*AHF
0068 A(79)=(SQRT(10.))*((B22/3.0)+((3.0*B24)/20.0))
0069 A(93)=A(79)
0070 A(108)=A(79)
0071 A(124)=A(79)
0072 A(141)=A(79)
0073 A(159)=A(79)
0074 A(86)=(SQRT(10.))*(CHF+BHF)/2.0
0075 A(98)=(SQRT(10.))*(CHF-BHF)/2.0
0076 A(100)=2.0*(CHF+BHF)
0077 A(113)=2.0*(CHF-BHF)
0078 A(115)=1.5*SQRT(2.)*(CHF+BHF)
0079 A(120)=1.5*SQRT(2.)*(CHF-BHF)
0080 A(131)=A(100)
0081 A(146)=A(113)
0082 A(148)=A(86)
0083 A(164)=A(98)
0084 FC=0.5*H-((8.0*B22)/3.0)+2.0*B04
0085 A(91)=FC+1.25*AHF
0086 A(105)=FC+C.75*AHF
0087 A(120)=FC+0.25*AHF
0088 A(136)=FC-0.25*AHF
0089 A(153)=FC-0.75*AHF
0090 A(171)=FC-1.25*AHF
0091 A(178)=SQRT(2.)*(B22-B24/4.0)
0092 A(198)=A(178)
0093 A(219)=A(178)
0094 A(241)=A(179)
0095 A(264)=A(179)
0096 A(288)=A(179)
0097 A(185)=A(40)
0098 A(203)=A(48)
0099 A(205)=A(115)
0100 A(224)=A(129)
0101 A(226)=2.25*(CHF+BHF)
0102 A(246)=2.25*(CHF-BHF)
0103 A(248)=A(205)
0104 A(269)=A(229)
0105 A(271)=A(185)
0106 A(293)=A(203)
0107 FD=-C.5*H-((8.0*B02)/3.0)+2.0*B04
0108 A(190)=FD-1.25*AHF
0109 A(210)=FD-0.75*AHF

```

0110 A(231)=FD-0.25*AHF
0111 A(253)=FD+C.25*AHF
0112 A(276)=FD+C.75*AHF
0113 A(300)=FD+1.25*AHF
0114 A(301)=(SQRT(5.)*B44)/5.0
0115 A(327)=A(301)
0116 A(354)=A(301)
0117 A(382)=A(301)
0118 A(411)=A(301)
0119 A(441)=A(301)
0120 A(313)=A(178)
0121 A(339)=A(178)
0122 A(366)=A(178)
0123 A(394)=A(178)
0124 A(423)=A(178)
0125 A(453)=A(178)
0126 A(320)=A(86)
0127 A(344)=A(98)
0128 A(346)=A(100)
0129 A(371)=A(113)
0130 A(373)=A(115)
0131 A(399)=A(129)
0132 A(401)=A(346)
0133 A(428)=A(371)
0134 A(430)=A(320)
0135 A(458)=A(344)
0136 FE=-1.5*H-((2.0*RO2)/3.0)-3.0*B04
0137 A(325)=FE-3.75*AHF
0138 A(351)=FE-2.25*AHF
0139 A(378)=FE-0.75*AHF
0140 A(406)=FE+0.75*AHF
0141 A(435)=FE+2.25*AHF
0142 A(465)=FE+3.75*AHF
0143 A(472)=A(301)
0144 A(504)=A(301)
0145 A(537)=A(301)
0146 A(571)=A(301)
0147 A(606)=A(301)
0148 A(642)=A(301)
0149 A(484)=A(79)
0150 A(516)=A(79)
0151 A(549)=A(79)
0152 A(583)=A(79)

```
C153 A(618)=A(79)
C154 A(654)=A(79)
C155 A(491)=A(23)
C156 A(521)=A(29)
C157 A(523)=A(31)
C158 A(554)=A(38)
C159 A(556)=A(40)
C160 A(588)=A(48)
C161 A(590)=A(31)
C162 A(623)=A(554)
C163 A(625)=A(491)
C164 A(659)=A(521)
C165 FF=-2.5*H+((10.0*B02)/3.0)+B04
C166 A(496)=FF-6.25*AHF
C167 A(528)=FF-3.75*AHF
C168 A(561)=FF-1.25*AHF
C169 A(595)=FF+1.25*AHF
C170 A(630)=FF+3.75*AHF
C171 A(666)=FF+6.25*AHF
C172 CALL EIGEN(A,R,N,MV)
C173 DO 260 I=1,N
C174 L=(I*I-I)/2
C175 S(I)=A(L)*1.0E-03
C176 HW=H*1.0E-03
C177 WRITE(3,180)HN,(S(J),J=1,36)
C178 180 FORMAT(/,6X,'H = ',F10.6,2X,'KILOGAUSS',/,6X,'EIGENVALUES',/,6X,
1F12.6,3X)
C179 H=H-C.5E+04
C180 IF(H-C.5E+04)11,21,13
C181 21 H=C.3E+04
C182 GO TO 13
C183 11 HA(1)=C.0
C184 DO 4 K=2,60
C185 4 HA(K)=HA(K-1)+0.16667E+C3
C186 DO 3 K=1,60
C187 FA=2.5*HA(K)+((10.0*B02)/3.0)+B04
C188 A(1)=FA+(25.0*AHF)/4.0
C189 A(3)=FA+(15.0*AHF)/4.0
C190 A(6)=FA+(5.0*AHF)/4.0
C191 A(10)=FA-(5.0*AHF)/4.0
C192 A(15)=FA-(15.0*AHF)/4.0
C193 A(21)=FA-(25.0*AHF)/4.0
C194 A(23)=1.25*(BHF+CHF)
```

0195 FB=1.5*HA(K)-((2.0*B02)/3.0)-3.0*B04
0196 A(28)=FB+(15.0*AHF)/4.0
0197 A(29)=1.25*(CHF-BHF)
0198 A(31)=(SQRT(10.))*(CHF+BHF))/2.0
0199 A(36)=FB+(9.0*AHF)/4.0
0200 A(38)=(SQRT(10.))*(CHF-RHF))/2.0
0201 A(40)=(3.0*SQRT(5.))*(CHF+BHF))/4.0
0202 A(45)=FB+0.75*AHF
0203 A(48)=(3.0*SQRT(5.))*(CHF-BHF))/4.0
0204 A(50)=A(31)
0205 A(55)=FB-0.75*AHF
0206 A(59)=A(38)
0207 A(61)=A(23)
0208 A(66)=FB-(9.0*AHF)/4.0
0209 A(71)=A(29)
0210 A(78)=FB-3.75*AHF
0211 A(79)=(SQRT(10.))*((B22/3.0)+((3.0*B24)/20.0))
0212 A(93)=A(79)
0213 A(108)=A(79)
0214 A(124)=A(79)
0215 A(141)=A(79)
0216 A(159)=A(79)
0217 A(86)=(SQRT(10.))*(CHF+BHF))/2.0
0218 A(98)=(SQRT(10.))*(CHF-BHF))/2.0
0219 A(100)=2.0*(CHF+BHF)
0220 A(113)=2.0*(CHF-BHF)
0221 A(115)=1.5*SQRT(2.)*(CHF+BHF)
0222 A(129)=1.5*SQRT(2.)*(CHF-BHF)
0223 A(131)=A(100)
0224 A(146)=A(113)
0225 A(148)=A(96)
0226 A(164)=A(98)
0227 FC=0.5*HA(K)-((8.0*B02)/3.0)+2.0*B04
0228 A(91)=FC+1.25*AHF
0229 A(105)=FC+0.75*AHF
0230 A(120)=FC+0.25*AHF
0231 A(136)=FC-0.25*AHF
0232 A(153)=FC-0.75*AHF
0233 A(171)=FC-1.25*AHF
0234 A(178)=SQRT(2.)*(B22-B24/4.0)
0235 A(198)=A(178)
0236 A(219)=A(178)
0237 A(241)=A(178)

0238 A(264)=A(178)
 0239 A(288)=A(178)
 0240 A(185)=A(40)
 0241 A(203)=A(48)
 0242 A(205)=A(115)
 0243 A(224)=A(129)
 0244 A(226)=2.25*(CHF+BHF)
 0245 A(246)=2.25*(CHF-BHF)
 0246 A(248)=A(205)
 0247 A(269)=A(229)
 0248 A(271)=A(185)
 0249 A(293)=A(203)
 0250 FD=-0.5*HA(K)-((9.0*B02)/3.0)+2.0*B04
 0251 A(190)=FD-1.25*AHF
 0252 A(210)=FD-0.75*AHF
 0253 A(231)=FD-0.25*AHF
 0254 A(253)=FD+0.25*AHF
 0255 A(276)=FD+0.75*AHF
 0256 A(300)=FD+1.25*AHF
 0257 A(301)=(SQRT(5.)*844)/5.0
 0258 A(327)=A(301)
 0259 A(354)=A(301)
 0260 A(382)=A(301)
 0261 A(411)=A(301)
 0262 A(441)=A(301)
 0263 A(313)=A(178)
 0264 A(339)=A(178)
 0265 A(365)=A(178)
 0266 A(394)=A(178)
 0267 A(423)=A(178)
 0268 A(453)=A(178)
 0269 A(320)=A(86)
 0270 A(344)=A(99)
 0271 A(346)=A(170)
 0272 A(371)=A(113)
 0273 A(373)=A(115)
 0274 A(399)=A(129)
 0275 A(401)=A(346)
 0276 A(428)=A(371)
 0277 A(430)=A(320)
 0278 A(458)=A(344)
 0279 FE=-1.5*HA(K)-((2.0*B02)/3.0)-3.0*B04
 0280 A(325)=FE-3.75*AHF

```
0281 A(351)=FE-2.25*AHF
0282 A(378)=FE-0.75*AHF
0283 A(406)=FE+0.75*AHF
0284 A(435)=FE+2.25*AHF
0285 A(465)=FE+3.75*AHF
0286 A(472)=A(301)
0287 A(504)=A(301)
0288 A(537)=A(301)
0289 A(571)=A(301)
0290 A(606)=A(301)
0291 A(642)=A(301)
0292 A(484)=A(79)
0293 A(516)=A(79)
0294 A(549)=A(79)
0295 A(583)=A(79)
0296 A(518)=A(79)
0297 A(654)=A(79)
0298 A(491)=A(23)
0299 A(521)=A(29)
0300 A(523)=A(31)
0301 A(554)=A(38)
0302 A(556)=A(40)
0303 A(588)=A(48)
0304 A(590)=A(31)
0305 A(623)=A(554)
0306 A(625)=A(491)
0307 A(659)=A(521)
0308 FF=-2.5*HA(K)+(10.0*B02)/3.0)+B04
0309 A(496)=FF-6.25*AHF
0310 A(528)=FF-3.75*AHF
0311 A(561)=FF-1.25*AHF
0312 A(595)=FF+1.25*AHF
0313 A(630)=FF+3.75*AHF
0314 A(666)=FF+6.25*AHF
0315 CALL EIGEN(A,R,N,MV)
0316 DD 270 I=1,36
0317 L=I+(I*I-I)/2
0318 S(I)=A(L)*1.0E-03
0319 P(I,K)=S(I)
0320 HG=HA(K)*1.0E-03
0321 X(K)=HG
0322 3 WRITE(3,180)HG,(S(I),I=1,36)
0323 GO TO 555
0324 END
```

```
C *****
C
C CALCULATION OF THE ENERGIES OF THE QUARTET STATES ABOVE THE
C GROUND STATE AS A FUNCTION OF THE CRYSTAL FIELD
C SPLITTING 10DQ .
C *****
C
C DIMENSION F(6),FF(6),E(3)
C REAL LAM
C WRITE(3,4)
4 FORMAT(1H1,/,10X,'ALL VALUES IN WAVENUMBERS')
C B=616.
C C=3968.
C LAM=-35.*B
C WRITE(3,3)C
3 FORMAT(///,10X,'C = ',F7.1)
C WRITE(3,5)B
5 FORMAT(///,10X,'B = ',F7.1)
C E(1)=-22.*B+5.*C-LAM
C E(2)=-2.*SQRT(3.)*B
C E(3)=-21.*B+5.*C-LAM
C CALL EIGEN(E,R,2,1)
C DQ=-100.
10 DQ=DQ+100.
C IF(DQ.GT.13000.)GO TO 15
C F(1)=-DQ-25.*B+6.*C-LAM
C F(2)=-3.*SQRT(2.)*B
C F(3)=-16.*B+7.*C-LAM
C F(4)=C
C F(5)=F(2)
C F(6)=DQ-25.*B+6.*C-LAM
C FF(1)=-DQ-17.*B+6.*C-LAM
C FF(2)=SQRT(6.)*B
C FF(3)=-22.*B+5.*C-LAM
C FF(4)=4.*B+C
C FF(5)=-FF(2)
C FF(6)=DQ-17.*B+6.*C-LAM
C CALL EIGEN(F,R,3,1)
C CALL EIGEN(FF,F,3,1)
C WRITE(3,6)DQ,F(1),F(3),F(6),FF(1),FF(3),FF(6),E(1),E(3)
6 FORMAT(//,10X,'10DQ = ',F10.3,/,10X,'EIGENVALUES',/,25X,3F10.3,/,
1,25X,3F10.3,/,25X,3F10.3)
C GO TO 10
15 RETURN
C END
```



```
0031      CALL EIGEN(F,R,3,1)
0032      CALL EIGEN(FF,R,3,1)
0033      WRITE(3,6)DQ,F(1),F(3),F(6),FF(1),FF(3),FF(6),X,E(1),E(3)
0034      6 FCRMAT(//,10X,10DQ = ,F10.3,/,10X, EIGENVALUES',/,25X,3F10.3,/,
          1,25X,3F10.3,/,25X,3F10.3)
          GO TO 10
0035      GO TO 10
0036      15 RETURN
0037      END
```



```

0035 B22=B22+8.*SQRT(1.5)*(SIN(TH)**2)*COS(2.*PI)/R**3
0036 B24=B24+SQRT(10.)*(SIN(TH)**2)*(7.*COS(TH)**2-1)*COS(2.*PI)/R**5*0
1.25
0037 B04C=B04C+C.5*(35.*COS(TH)**4-30.*COS(TH)**2+3.)/R**5*0.25
0038 B44C=B44C+8.*SQRT(35./32.)*(SIN(TH)**4)*COS(PI)**4/R**5
0039 B04NC=B04C
0040 B44NC=B44NC+D.25*SQRT(70.)*(SIN(TH)**4)*COS(4.*PI)/R**5*0.25
0041 GO TO 3
0042 15 APH=B04C/B44C
0043 B04P=B04NC-APH*B44NC
0044 DW=-((LAMBDA**2)*AR2*(B02*A1)**2)/(70.*DDDS*0P5**2)
0045 DWC=-((LAMBDA**2)*AR2*(B02*A1)**2*(ABS(PAA+4.*PAB/7.))**2)/(70.*D
IDS))
0046 XX=AP4*((LAMBDA**2)*PAG*(2.*PAA-PAB))
0047 DBO=B04P*A2*(SQRT(5.)/36.)*XX
0048 FRO=-B24*A2*(SQRT(2.)/6.)*XX
0049 DDDS=2.1044*B02**2
0050 FSS=-0.09269*R22
0051 DSS=-0.07306*B02
0052 D=DW+DWC+DR0+DDDS+DSS
0053 E=ERO+ESS
0054 WRITE(3,4)B02,B22,B24,B04P,B04C,B04NC
0055 4 FORMAT(1H1,10X,'CRYSTAL FIELD PARAMETERS',//,20X,'B02 = ',E15.8,/,
120X,'B22 = ',E15.8,/,20X,'B24 = ',E15.8,/,20X,'B04P = ',E15.8,/,20
2X,'B04C = ',E15.8,/,20X,'B04NC = ',E15.8)
0056 WRITE(3,5)DW,DWC,DBO,DDDS,DSS,FSS,D,E
0057 5 FORMAT(///,10X,'ZERO-FIELD SPLITTING',//,20X,'DW = ',E15.8,/,20X,'
1DWC = ',E15.8,/,20X,'DBO = ',E15.8,/,20X,'FSS = ',E15.8,/,20X,'DSS = ',E15.8,/,20X,'TOTAL F = ',E15.8,/,20X,'CM-1',)
2S = ',E15.8,/,20X,'DSS = ',E15.8,/,20X,'ESS = ',E15.8,/,20X,'TOTAL F = ',E15.8,/,20X,'CM-1',)
3L D = ',E15.8,/,20X,'TOTAL F = ',E15.8,/,20X,'CM-1',)
0058 RETURN
0059 END

```

References

1. R. G. Burns, Mineralogical Applications of Crystal Field Theory (Cambridge University Press, London) 1970.
2. S. Koide and M. H. L. Pryce, Phil. Mag. 3, 607 (1958)
3. J. Owen, Proc. Roy. Soc. A227, 183 (1955).
4. J. S. Van Wieringen, Disc. Faraday Soc. 19, 118 (1955)
5. O. Maturuma, J. Phys. Soc. Japan 14, 108 (1959)
6. J. C. M. Henning, Phys. Letters 24A, 40 (1967)
7. E. Simanek and K. A. Muller, J. Phys. Chem. Solids 31, 1027 (1970).
8. L. Pauling, The Nature of the Chemical Bond (Cornell University Press, Ithaca, New York) 1960.
9. J. C. Phillips, Rev. Mod. Phys. 42, 317 (1970).
10. M. Giglio, Acta. Cryst. 11, 789 (1958)
11. I. M. Rumanova and G. I. Malitskaya, Soviet Phys. Crystallography (Eng. Trans.) 4, 481 (1960).

12. D. J. Sutor, Acta. Cryst. 23, 418 (1967)
1
13. L. H. Cohen and P. H. Ribbe, Am. Min. 51 1755 (1966)
14. A. Whitaker and J. W. Jeffrey, Acta. Cryst. B26, 1429 (1970)
15. A. Whitaker and J. W. Jeffrey, Act. Cryst. B26, 1440 (1970)
16. B. N. Figgis, Introduction to Ligand Fields (Interscience, New York) 1966.
17. G. W. Pratt and R. Coelho, Phys. Rev. 116 281 (1959)
18. a) G. Racah, Phys. Rev. 62, 438 (1942); b) 63, 367 (1942);
c) 76, 1352 (1949).
19. E. U. Condon and G. H. Shortley, The Theory of Atomic Spectra (Cambridge University Press, London) 1953.
20. L. J. Heidt, G. F. Koster and A. M. Johnson, J. Am. Chem. Soc. 80, 6471 (1959)
21. W. Low, Paramagnetic Resonance in Solids (Academic Press, New York) 1960.
22. Y. Tanabe and S. Sugano, J. Phys. Soc. Japan 9, 753 (1954).
23. J. W. Stout, J. Chem. Phys. 31 709 (1959)
24. A. Abragam and M. H. L. Pryce, Proc. Roy. Soc. A205, 135 (1951)

25. R. Orbach and E. Simanek, Phys. Rev. 158, 310 (1967).
26. M. H. L. Pryce, Proc. Roy. Soc. A63, 25 (1950).
27. V. M. Vinokurov, M. M. Zaripov, and V. G. Stepanov, Soviet Phys. Solid State (Eng. Trans.) 6, 870 (1964)
28. R. Orbach, Proc. Roy. Soc. A264, 458 (1961)
29. H. Bethe, Ann. Physik 3, 133 (1929)
30. J. H. Van Vleck and W. G. Penney, Phil. Mag. 17, 961 (1934)
31. H. Watanabe, Progr. Theoret. Phys. (Kyoto) 18, 405 (1957)
32. J. R. Gabriel, D. F. Johnston, and M. S. D. Powell. Proc. Roy. Soc. A264, 503 (1961)
33. A. M. Leushin, Soviet Phys. Solid State (Eng. Trans.) 5, 2477 (1964)
34. H. Watanabe, J. Phys. Chem. Solids 25, 1471 (1964).
35. A. Van Heuvelen, J. Chem. Phys. 46, 4903 (1967)
36. B. G. Wybourne, J. Chem. Phys. 43, 4506 (1965)
37. M. Blume and R. Orbach, Phys. Rev. 127, 1587 (1962)
38. a) R. R. Sharma, T. P. Das, and R. Orbach, Phys. Rev. 149, 257 (1966);
b) 155, 338 (1967); c) 171, 378 (1968).

39. A. Manoogian, J. Phys. E.: Scientific Instr. 4, 263 (1971).
40. V. M. Vinokurov and R. S. Tuhvatullin, Geokhimiya 4, 496 (1968)
41. B. Bleaney and D. J. E. Ingram, Proc. Roy. Soc. A205, 336 (1951)
42. W. Low, Phys. Rev. 105, 793 (1957).
43. A. Manoogian and Y. Hsu, Can. J. Phys. 47, 1869 (1969).
44. A. G. Danilov and A. Manoogian, Can. J. Phys. 47, 839 (1969)
45. A. Manoogian, Can. J. Phys. 46, 129 (1968)
46. T. Takeda, J. Phys. Soc. Japan 23, 1314 (1967)
47. W. A. Pieczonka, H. F. Petch and A. B. McLay, Can. J. Phys., 39 145 (1961)
48. I. J. Fritz and L. Yatmus, Phys. Rev. 173, 445 (1968)
49. V. M. Vinokurov, M. M. Zaripov and V. G. Stepanov, Soviet Phys. Solid State (Eng. Trans.) 6, 866 (1964)
50. A. Chatelain and R. A. Weeks, J. Chem. Phys. 52, 5682 (1970)
51. B. Milsch and W. Windsch, Phys. Stat. Sol. 31 K79 (1969)
52. L. E. Orgel, J. Chem. Phys. 23, 1004 (1955)

53. P. G. Manning, *Can. Min.* 9, 237 (1967)
54. G. H. Faye, *Can. J. Earth Sci.*, 5, 31 (1968)
55. E. M. Wray and J. W. Allen, *J. Phys. C.: Solid St. Phys.* 4, 512 (1971)
56. R. Stevenson, *Can. J. Phys.*, 43, 1732 (1965)
57. A. Mehra and P. Venkatasivartu, *J. Chem. Phys.*, 45 3381 (1966)
58. C. K. Jorgensen, *Acta. Chem. Scand.* 11 53 (1957)
59. D. D. Sell, R. L. Greene and R. G. White, *Phys. Rev.* 158, 489 (1967).

CURRICULUM VITAE

Name: Barry Richard KIGGINS

Born: OTTAWA, Ontario, Canada
10th July, 1948

EDUCATED:

| | | |
|-------------|----------------------|-----------|
| High School | St. Joseph's, Ottawa | 1960-65 |
| University | University of Ottawa | 1965-1970 |
| Degree | B.Sc.(Hons.) Physics | 1970 |

CURRICULUM VITAE

Name: Barry Richard KIGGINS

Born: OTTAWA, Ontario, Canada
10th July, 1948

EDUCATED:

| | | |
|-------------|-----------------------|-----------|
| High School | St. Joseph's, Ottawa | 1960-65 |
| University | University of Ottawa | 1965-1970 |
| Degree | B.Sc. (Hons.) Physics | 1970 |